Optimizing Coded Excitation for Model-Based Ultrasound Imaging With Unfocused Transmissions

Didem Dogan, Lixiang Zhu, Yuyang Hu, Johannes G. Bosch, *Member, IEEE*, Pieter Kruizinga, and Geert Leus, *Fellow, IEEE*

***Abstract*—Ultrafast imaging, which uses unfocussed transmissions to form images, provides very high frame rates at the cost of low signal-to-noise ratio (SNR). This loss of SNR becomes especially apparent when imaging deeper structures. Ultrafast imaging is mostly used in combination with Doppler processing. Even if we apply tissue-separation filters, they lead to significant energy loss and decrease the SNR. Previous work showed that this loss in SNR and, hence, penetration depth can be partially regained using coded transmissions. However, these codes are mostly either standard or randomly generated and can be improved with a design rooted in an optimization scheme. To address this limitation, we design an optimized code tailored to ultrasound imaging with unfocused transmissions represented by a generalized encoding matrix in a linear signal model. We employ the minimization of the Cramér-Rao lower bound (CRB) over the unknown coding matrix as a way to optimize the code. Due to the high computational cost of the resulting optimization problems, we also introduce a trace-constraint optimization problem based on the Fisher information matrix (FIM). Simulation results show that the optimized code provides higher SNR in deep image regions than previously tested coding schemes such as the Barker code, albeit with a trade-off for decreased resolution. On the other hand, the application of least-squares QR (LSQR) mitigates this resolution degradation. Lastly, the optimized code was tested in simulations using a numerical model of a clinical transducer setting, demonstrating its potential for higher SNR in ultrafast Doppler imaging.**

***Index Terms*—Coded excitation, Cramér-Rao lower bound (CRB), fisher information matrix (FIM), unfocused transmissions.**

I. Introduction

DOPPLER ultrasound imaging is a well-established technique widely used for imaging blood flow inside the human body, leveraging the principles of ultrasound and the interaction of mechanical pressure waves with tissue and red blood cells [1], [2]. Unfocused transmissions are advantageous for Doppler ultrasound compared to conventional ultrasound imaging [3]. The latter employs focused ultrasonic waves and sends a single focused wave during each transmission, reconstructing one image line at a time. However, this might not achieve a high sampling frequency and could result in inaccuracies for Doppler imaging [4]. In contrast, in unfocused transmissions such as plane-wave imaging, receivers capture the backscattered echoes from the entire imaging area. This enables the reconstruction of a full image from a single transmission using beamforming. It can obtain much more images compared to conventional ultrasound for the same number of firings and acquisition time.

Unfocussed transmissions trade image quality (specifically SNR) for temporal resolution, which is beneficial for Doppler imaging [5]. This gain allows for novel imaging applications such as functional ultrasound [4], pulse wave velocity imaging [6], etc. Although they also notably trade-off (reduce) spatial resolution, we are particularly interested in imaging blood flow inside the brain, where the SNR is of paramount importance. A higher SNR contributes to a high-quality image, enhancing diagnostic capabilities in clinical applications [7]. Unfocused transmissions face challenges in visualizing vasculature due to a low SNR. Echo signals from blood cells are considerably weaker than surrounding tissue. This leads to limitations in visualizing small blood vessels and deep areas.

There are advanced filtering methods for visualization of the microvasculature especially at greater depths. While some of these filters can be classified as beamforming methods, many others can be categorized as post-processing methods for detailed visualization. Examples of beamforming approaches include MVDR [8], LSQR (Least Squares QR, an iterative algorithm used for solving large linear systems of equations) [9], sparse reconstruction methods [10], and deep learning-based methods [11]. In terms of post-processing, methods like SVD filtering [12] and super-resolution techniques such as TMSBL [13] and SUSHI [14] improve the quality of the beamformed image and enable better visualization at deeper levels. However, these methods often face challenges related to computational complexity, particularly when applied to real-time imaging.

It is also observed in ultrasound literature that applying coded excitation [15], [16], [17], [18], [19], which means sending out longer encoded pulses, can enhance the SNR of ultrasound images and improve the penetration depth. Coded excitation achieves a high main lobe-to-side lobe ratio after pulse compression, with an axial resolution comparable to or slightly worse than a single short pulse. Note that pulse compression

Received 30 January 2025; revised 18 April 2025; accepted 28 April 2025. Date of publication 1 May 2025; date of current version 14 May 2025. This work was supported by the TOUCAN under Project 17208 of the research programme TTW-OTP which is funded by the Dutch Research Council (NWO). The associate editor coordinating the review of this article and approving it for publication was Prof. Andreas Hauptmann. *(Corresponding author: Didem Dogan.)*

Didem Dogan, Lixiang Zhu, and Geert Leus are with the Signal Processing Systems (SPS), Delft University of Technology, 2628 CD Delft, The Netherlands (e-mail: d.doganbaskaya-1@tudelft.nl).

Yuyang Hu and Johannes G. Bosch are with the Department of Cardiology, Erasmus Medical Center Thorax Biomedical Engineering, 3015 GD Rotterdam, The Netherlands.

Pieter Kruizinga is with the Department of Neuroscience, Erasmus Medical Center, 3015 GD Rotterdam, The Netherlands.

Digital Object Identifier 10.1109/TCI.2025.3566224

is a signal processing technique where a long-duration coded pulse is transmitted and its echo is processed via decoding filtering to compress energy into a narrow peak [20], [21]. The design of coded excitation pulses typically utilizes frequency or phase encoding techniques based on the impulse response of the transducer [22]. Frequency encoding involves linearly modulating a carrier signal frequency, often achieved through linear frequency modulation (FM), also known as chirp excitation [16]. On the other hand, phase encoding is achieved by modulating the phase of the transmitted pulse, such as linear phase modulation and bi-phase modulation [15]. In linear phase modulation, the phase changes linearly with time across the pulse duration. This creates a smooth phase transition and can contribute to the signal's resilience against distortion and interference. In bi-phase modulation, the transmitted pulse is encoded with either a 0-degree shift (represented by 1) or a 180-degree shift (represented by -1).

The two commonly used bi-phase modulation sequences are the Golay and Barker codes, which have found extensive applications in ultrasound imaging thanks to their favorable autocorrelation properties and ability to generate high-quality images with improved signal-to-noise ratio [23], [24]. A Barker code is a binary sequence that leads to a high main lobe-to-side lobe ratio after matched filtering, with good autocorrelation properties. However, existing Barker codes only have specific lengths, restricting the total transmitted energy. The Golay code consists of a pair of finite equal-length binary sequences. Unlike single transmit signals like Barker codes, which exhibit range side lobes after pulse compression, the Golay pair is designed to cancel out these range side lobes. However, the drawback of Golay pairs is that the frame rate will be halved since it requires two transmissions to obtain a single image. Note that these two transmissions are added to cancel out the side lobes. A major weakness of Golay code pairs is incomplete cancellation caused by target motion between transmissions, even when complementary orthogonal codes are used. This problem has been tackled in [25] by transmitting two pairs of mutually complementary orthogonal codes, which can achieve the same frame rate as a single transmission code.

Instead of applying the same code for every transmitting element, the random code is an alternative to Barker and Golay encoding, incorporating the time and space domains [26]. Instead of transducer elements transmitting the same encoded pulse, this method excites each element with a different randomly encoded pulse. The resulting randomly transmitted waves constructively and destructively interfere in the imaging area, creating spatio-temporal interference patterns. This leads to low pixel-to-pixel correlations, which might yield a high-resolution image. However, the SNR improvement is quite limited compared to Barker and Golay codes. Furthermore, there are also complete complementary codes that offer better side lobe suppression and higher SNR improvement compared to random codes [27]. Hence, they are more effective for high-quality imaging while maintaining low pixel-to-pixel correlations.

Coded excitation in ultrasound imaging can be refined using diverse methods. One promising way involves investigating hybrid coding techniques, combining different coding sequences to combine their strengths. For instance, [28] suggests the convolution of Barker and Golay codes to effectively mitigate side lobe levels, leading to a notable increase in SNR. Similarly, [29] introduces chirp-modulated Golay codes, integrating orthogonal binary codes with a chirp, which results in a substantial enhancement. Another approach is integrating advanced signal processing algorithms to decode and reconstruct received echoes efficiently. Decoding filtering techniques, such as mismatched or adaptive filters [30], [31], play a critical role in balancing side lobe suppression and SNR gain during pulse compression. For instance, the work [32] uses a finite impulse response (FIR) filter, to decode echoes transmitted with Barker codes, effectively suppressing the side lobe energy at the expense of decreased SNR. This approach further facilitates the design of longer Barker codes using Kronecker products, enabling applications such as functional ultrasound neuroimaging, but it may degrade the autocorrelation properties.

There is a potential for utilizing optimized code design to enhance SNR in ultrasound imaging with unfocused transmissions. While substantial research has been dedicated to optimized code design in the radar domain, emphasizing robustness and high-resolution [33], [34] and demonstrating significant improvements in radar detectability, a notable gap exists for unfocused transmissions in ultrasound imaging. Therefore, this paper explores optimized code sequences for ultrasound imaging with unfocused transmissions. We first present a linear signal model where the code sequences appear in a coding matrix. To optimize this coding matrix, we employ the minimization of the Cramér-Rao lower bound (CRB) [35] as a proxy to minimize the mean square error [36]. In that sense, the minimization of the maximum eigenvalue, determinant, and trace of the CRB matrix has been proposed to find the optimized encoding matrix for a specific imaging area [37]. Since the original problem is non-convex, some relaxations are imposed to ensure a feasible solution [38]. The drawback of this approach is its computational complexity and memory challenge for large imaging areas. A suboptimal formulation is proposed to address this by maximizing the trace of the Fisher information matrix (FIM) instead of minimizing the trace of the CRB. Fortunately, the maximization of the trace of the FIM results in a small-scale problem that can be solved by finding the eigenvector of a small-sized matrix corresponding to the largest eigenvalue. Therefore, the proposed approach is computationally more efficient.

The rest of the paper is organized as follows: Section II presents the signal model and the associated image reconstruction. The subsequent section, Section III, focuses on articulating the optimization methods applicable to the encoding matrix. Further, Section IV shows the results, delving into the application scenario for the proposed method and discussing its limitations. Conclusions are drawn in Section VI.

II. Signal Model

In this work, model-based beamforming is employed instead of the conventional delay-and-sum (DAS) approach. In our approach, each transmitter sends different pulses, while DAS is useful in the case where all transmitters share the same coding pattern. Model-based beamforming provides more flexibility in

handling the diverse coded excitation scheme. In model-based ultrasound imaging, we first construct the image formation model and represent this in the form of a matrix-vector multiplication [10]. In the ultrasound imaging system, there are N elements where all the elements transmit and receive the backscattered signal. The imaging area is discretized into a grid of M pixels. Using the Born approximation [39], each measurement is represented as a linear combination of the pulse-echo signals from the scatterers [40] weighted by their scattering coefficient. Throughout this paper, we will work in the frequency domain instead of the time domain since it allows for faster computation. More specifically, we only consider a limited set of F frequencies given by $\Omega = \{\omega_1, \omega_2, \ldots, \omega_F\}$, which are assumed equidistant and within the positive side of the frequency spectrum. Defining $z_j[\omega]$ as the signal received by the jth element at frequency ω, we can write

$$z_j[\omega] = \sum_{m=1}^{M} s_m \sum_{i=1}^{N} g_{j,m,i}[\omega] u_i[\omega]. \tag{1}$$

Here, s_m represents each pixel's unknown reflection coefficient, and $u_i[\omega]$ represents the excitation pulse sent by element i at frequency ω. Furthermore, $g_{j,m,i}[\omega]$ is the overall Green's function for the wave propagating from the transmitting element i to pixel m and from the pixel m to the receiving element j. The computation of Green's function considers factors such as the distance between the transmitting/receiving elements and each pixel, attenuation during propagation in the tissue, and the impulse responses of the transducers. The overall function $g_{j,m,i}[\omega]$ is given by

$$g_{j,m,i}[\omega] = \frac{h_t[\omega] h_r[\omega]}{4\pi(d_{i,m} + d_{m,j})} \exp\Big(-j\frac{\omega}{v_0}(d_{i,m} + d_{m,j})\Big), \tag{2}$$

where $h_t[\omega]$ and $h_r[\omega]$ respectively correspond to the known transmit and receive impulse responses of the transducer, $d_{i,m}$ denotes the distance from the transmitting element i to pixel m, and $d_{m,j}$ is the distance covered by the backscattered signal from pixel m to sensor j. Further, v_0 corresponds to the speed of sound in the medium. The denominator in (2) stands for the geometric spreading of the pressure field, considering the entire distance the wave travels from the source to the pixel and back to the sensor. The exponential term in (2) represents the phase shift caused by the delay from the source to the pixel and back to the sensor.

Note that the excitation pulse $u_i[\omega]$ in (1) depends on the transmitting elements. For this scenario, we consider a case where all N elements transmit longer pulses consisting of an equal number K of base pulses. Every base pulse is amplitude and bi-phase encoded with a weight denoted by $c_{i,k}$. Hence, the excitation pulse $u_i[\omega]$ at transmitting element i and frequency ω can be written as

$$u_i[\omega] = \sum_{k=1}^{K} c_{i,k} p_k[\omega] = \mathbf{c}_i^{\mathsf{T}} \mathbf{p}[\omega], \tag{3}$$

where $p_k[\omega]$ denotes the kth base pulse. The relation between two consecutive base pulses is $p_{k+1}[\omega] = p_k[\omega] e^{-j\omega\tau}$ where τ is the delay between two base pulses. Further, $\mathbf{p}[\omega] = [p_1[\omega], p_2[\omega], \ldots, p_K[\omega]]^{\mathsf{T}}$ is the base pulse vector and $\mathbf{c}_i = [c_{i,1}, c_{i,2}, \ldots, c_{i,K}]^{\mathsf{T}}$ is the amplitude and bi-phase code related to transmit element i. Here, we also concatenate the $\mathbf{c}_i$'s as $\mathbf{C} \in \mathbb{R}^{N\times K}$, which is called the encoding matrix, i.e., $\mathbf{C} = [\mathbf{c}_1, \mathbf{c}_2, \ldots, \mathbf{c}_N]^{\mathsf{T}}$.

The measurements from all elements are stacked in a vector $\mathbf{z}[\omega] \in \mathbb{C}^N$, and the part related to the Green's functions can be stored in a matrix $\mathbf{A}_\mathbf{c}[\omega]$. The measurement model for all elements at frequency ω is then expressed as

$$\mathbf{z}[\omega] = \begin{bmatrix} z_1[\omega] \\ \vdots \\ z_N[\omega] \end{bmatrix} = \mathbf{A}_\mathbf{c}[\omega]\mathbf{s}, \tag{4}$$

where the mth entry of the vector $\mathbf{s} \in \mathbb{R}^M$ is $[\mathbf{s}]_m = s_m$ and the (j,m)th entry of the matrix $\mathbf{A}_\mathbf{c}[\omega] \in \mathbb{C}^{N\times M}$ is written as

$$[\mathbf{A}_\mathbf{c}[\omega]]_{j,m} = \sum_{i=1}^{N} g_{j,m,i}[\omega] \mathbf{c}_i^{\mathsf{T}} \mathbf{p}[\omega] = \mathbf{g}_{j,m}^{\mathsf{T}}[\omega] \mathbf{C}\mathbf{p}[\omega], \tag{5}$$

where $\mathbf{g}_{j,m}[\omega] = [g_{j,m,1}[\omega], \ldots, g_{j,m,N}[\omega]]^{\mathsf{T}}$. Now we can also write $\mathbf{A}_\mathbf{c}[\omega]$ in (4) as follows

$$\begin{aligned} \mathbf{A}_\mathbf{c}[\omega] &= \begin{bmatrix} \mathbf{g}_{1,1}^{\mathsf{T}}[\omega] & \cdots & \mathbf{g}_{1,M}^{\mathsf{T}}[\omega] \\ \vdots & \ddots & \vdots \\ \mathbf{g}_{N,1}^{\mathsf{T}}[\omega] & \cdots & \mathbf{g}_{N,M}^{\mathsf{T}}[\omega] \end{bmatrix} [\mathbf{I}_M \otimes (\mathbf{C}\mathbf{p}[\omega])] \\ &= \mathbf{G}[\omega][\mathbf{I}_M \otimes (\mathbf{C}\mathbf{p}[\omega])]. \end{aligned} \tag{6}$$

where $\mathbf{I}_M$ is an $M \times M$ identity matrix. It is clear from (6) that $\mathbf{A}_\mathbf{c}[\omega]$ is linear in every element of the encoding matrix $\mathbf{C}$. As a result, (6) can be written as

$$\mathbf{A}_\mathbf{c}[\omega] = \sum_{n=1}^{N} \sum_{k=1}^{K} c_{n,k} \mathbf{A}_{n,k}[\omega], \tag{7}$$

where $\mathbf{A}_{n,k}[\omega] \in \mathbb{C}^{N\times M}$ is given by

$$\mathbf{A}_{n,k}[\omega] = \mathbf{G}[\omega][\mathbf{I}_M \otimes (\mathbf{E}_{n,k}\mathbf{p}[\omega])], \tag{8}$$

with $\mathbf{E}_{n,k} \in \mathbb{R}^{N\times K}$ a matrix with only one non-zero entry, i.e., $[\mathbf{E}_{n,k}]_{n,k} = 1$. The matrix $\mathbf{E}_{n,k}$ basically selects which code entry is active.

Finally, all the frequency components are computed and concatenated vertically. Adding zero-mean white Gaussian noise with variance σ^2 to the model, this leads to

$$\mathbf{z} = \begin{bmatrix} \mathbf{z}[\omega_1] \\ \vdots \\ \mathbf{z}[\omega_F] \end{bmatrix} = \begin{bmatrix} \mathbf{A}_\mathbf{c}[\omega_1] \\ \vdots \\ \mathbf{A}_\mathbf{c}[\omega_F] \end{bmatrix} \mathbf{s} + \mathbf{n} = \mathbf{A}_\mathbf{c}\mathbf{s} + \mathbf{n}. \tag{9}$$

Here, $\mathbf{z} \in \mathbb{R}^{FN}$ contains all measured samples from the array transducer in the frequency domain and $\mathbf{A}_\mathbf{c} \in \mathbb{R}^{FN\times M}$ collects as columns the impulse responses related to the different pixels. Here, $\mathbf{n} \in \mathbb{R}^{FN}$ represents the additive white Gaussian noise. Due to (7) we can write

$$\mathbf{A}_\mathbf{c} = \sum_{n=1}^{N} \sum_{k=1}^{K} c_{n,k} \mathbf{A}_{n,k}, \tag{10}$$

where

$$\mathbf{A}_{n,k} = \begin{bmatrix} \mathbf{A}_{n,k}[\omega_1] \\ \vdots \\ \mathbf{A}_{n,k}[\omega_F] \end{bmatrix}.$$

For simplicity, we will group the two indices n and k into a single index p as $p = (k-1)N + n$, where $p = 1, 2, \ldots, NK$. In this context, we will also define $c_{(k-1)N+n} = c_{n,k}$ and $\mathbf{A}_{(k-1)N+n} = \mathbf{A}_{n,k}$, which allows us to rewrite (10) as

$$\mathbf{A_c} = \sum_{p=1}^{NK} c_p \mathbf{A}_p, \tag{11}$$

Finally note that we can view c_p as the pth entry of the vector $\mathbf{c} = \text{vec}(\mathbf{C})$, where vec(.) vectorizes a matrix columnwise.

In the remainder of this paper, coded excitation techniques are generalized using the encoding matrix $\mathbf{C}$. The rows of $\mathbf{C}$ are identical for Barker and Golay codes, as the same signal is transmitted from all transducers while the elements are randomly generated for the random code case. For all those schemes, the entries of $\mathbf{C}$ are 1 or -1. In addition to bi-phase encoding, we also consider amplitude encoding in the proposed optimized coding scheme, as it has proven its advantages in radar applications [41]. The modulus of each entry in $\mathbf{C}$ is the weight for amplitude encoding, while its polarity stands for the phase encoding of the transmitted ultrasound pulses.

A. Imaging Techniques

Before optimizing the code, let us present imaging methods that solve (9). The simplest one is matched filtering, which maximizes the SNR under additive Gaussian noise and has the following solution:

$$\hat{\mathbf{s}} = \mathbf{A}_\mathbf{c}^\mathsf{H} \mathbf{z}. \tag{12}$$

Secondly, least squares estimation can be considered, which minimizes the sum of squared differences between the measurement vector $\mathbf{z}$ and the modeled measurement vector based on the estimated vector $\mathbf{s}$. It has the following closed-form solution:

$$\hat{\mathbf{s}} = (\mathbf{A}_\mathbf{c}^\mathsf{H} \mathbf{A}_\mathbf{c})^{-1} \mathbf{A}_\mathbf{c}^\mathsf{H} \mathbf{z}, \tag{13}$$

which only holds when $\mathbf{A_c}$ is full rank.

Note that matched filtering (12) will be the main technique employed in this work, thanks to its efficiency and ease of implementation. On the other hand, the least squares estimation in (13) has a large inverse, and its computational complexity is significantly high. Instead of solving the large inverse, an iterative LSQR algorithm will be used [9].

III. Optimization of the Encoding Matrix

Based on the earlier developed linear measurement model, we are now ready to find the optimal coded excitation scheme. Therefore, we first focus on estimating the image $\mathbf{s}$, and we then optimize the related estimation error for $\mathbf{s}$ with respect to $\mathbf{c}$ (the vectorized version of the coded excitation matrix $\mathbf{C}$). Suppose $\mathbf{s}$ is deterministic and unknown. In that case, we can estimate $\mathbf{s}$ using an unbiased estimator leading to an error covariance matrix $\mathbf{R_e} = \mathbb{E}(\mathbf{e}\mathbf{e}^\mathsf{H})$ [36], with $\mathbf{e} = \mathbf{s} - \hat{\mathbf{s}}$. This could be any of the previously considered estimators, including (if needed) a proper normalization for making the estimator unbiased. The trace of the error covariance matrix $\mathbf{R_e}$ yields the mean square error (MSE) of the estimator [36]. For any unbiased estimator, the error covariance matrix $\mathbf{R_e}$ is bounded below by the Cramér–Rao lower bound (CRB) matrix. So, instead of finding an expression for $\mathbf{R_e}$ related to a specific unbiased estimator, we will make use of the CRB matrix, which is often easier to derive. We thereby also remark that the CRB matrix is the inverse of the Fisher information matrix (FIM) $\mathbf{F}$, which quantifies how much information a dataset provides about the parameter of interest. So in general, we have $\mathbf{R_e} \succeq \mathbf{F}^{-1}$, where $\mathbf{F}$ could potentially depend on the unknown image $\mathbf{s}$. For our specific data model, which is a linear additive Gaussian model, the FIM is independent of $\mathbf{s}$ and is given by

$$\mathbf{F} = \sigma^{-2} \mathbf{A}_\mathbf{c}^\mathsf{H} \mathbf{A_c}. \tag{14}$$

As can be seen, it does not depend on $\mathbf{s}$ but it does depend on the code $\mathbf{c}$. We make this explicit by writing $\mathbf{F}(\mathbf{c})$ instead of $\mathbf{F}$.

A. CRB Minimization

There are three ways of minimizing the CRB matrix: minimization of the largest eigenvalue of the CRB matrix (Eig-Opt), minimization of the determinant of the CRB matrix (Det-Opt), or minimization of the trace of the CRB matrix (Trace-Opt) [37].

a) Eig-Opt: We first formulate the problem for Eig-Opt, which minimizes the largest eigenvalue of the CRB matrix. Note that using the maximum eigenvalue ensures that the CRB is minimized on all elements simultaneously. On the other hand, they might compensate for each other within the trace or determinant. In that sense, Eig-Opt can be more efficient for minimizing the CRB [37]. The Eig-Opt problem can be written as follows:

$$\begin{aligned} \min_{\mathbf{c}} \quad & \lambda_{\max}(\mathbf{F}^{-1}(\mathbf{c})) \\ \text{s.t.} \quad & ||\mathbf{c}||_2^2 = 1, \end{aligned} \tag{15}$$

where $\lambda_{\max}(\mathbf{F}^{-1}(\mathbf{c}))$ is the maximum eigenvalue of $\mathbf{F}^{-1}(\mathbf{c})$. Note that minimizing the maximum eigenvalue of the CRB matrix is equivalent to maximizing the minimum eigenvalue of its inverse. As such, we can also write

$$\begin{aligned} \max_{\mathbf{c}} \quad & \lambda_{\min}(\mathbf{A}_\mathbf{c}^\mathsf{H} \mathbf{A_c}) \\ \text{s.t.} \quad & ||\mathbf{c}||_2^2 = 1, \end{aligned} \tag{16}$$

where $\lambda_{\min}(\mathbf{F}^{-1}(\mathbf{c}))$ is the minimum eigenvalue of $\mathbf{F}^{-1}(\mathbf{c})$. Here, (16) is equivalent to

$$\begin{aligned} \max_{\lambda, \mathbf{c}} \quad & \lambda \\ \text{s.t.} \quad & \mathbf{A}_\mathbf{c}^\mathsf{H} \mathbf{A_c} - \lambda \mathbf{I}_M \succeq \mathbf{0}, \\ & ||\mathbf{c}||_2^2 = 1, \end{aligned} \tag{17}$$

where the first constraint is not linear in $\mathbf{c}$, and the problem in (17) is thus not convex. More specifically, we can write

$$\begin{aligned} \mathbf{A}_\mathbf{c}^\mathsf{H} \mathbf{A_c} &= \left(\sum_{p=1}^{NK} c_p \mathbf{A}_p \right)^\mathsf{H} \left(\sum_{q=1}^{NK} c_q \mathbf{A}_q \right) \\ &= \sum_{p=1}^{NK} \sum_{q=1}^{NK} c_p^* c_q \mathbf{A}_p^\mathsf{H} \mathbf{A}_q, \end{aligned} \tag{18}$$

where c_p^* represents the complex conjugate of c_p. Solving nonconvex problems can be challenging due to the potential of traditional optimization algorithms getting trapped in local optima or encountering convergence issues. As a result, some relaxation is introduced to turn the nonconvex problem into a convex one. Here, a common relaxation technique is employed, which involves absorbing the quadratic term $c_p^* c_q$ into a single

variable $C_{p,q}$ [36]. As such, (18) can be transformed into

$$\mathbf{A}_{\mathbf{c}}^{\mathsf{H}}\mathbf{A}_{\mathbf{c}} = \sum_{p=1}^{NK}\sum_{q=1}^{NK} C_{p,q}\mathbf{A}_p^{\mathsf{H}}\mathbf{A}_q, \tag{19}$$

which is linear in $C_{p,q}$ instead of quadratic in c_p. Introducing the matrix $\mathcal{C} \in \mathbb{C}^{NK\times NK}$ with $[\mathcal{C}]_{p,q} = C_{p,q}$, the equivalence between (18) and (19) only holds when $\mathcal{C} = \mathbf{c}\mathbf{c}^{\mathsf{H}}$. This requires $\mathcal{C}$ to be a rank-one matrix, and this constraint is not convex. One way to relax this rank-one constraint is by replacing it with $\mathcal{C} \succeq \mathbf{0}$. Defining $\mathbf{A} = [\mathbf{A}_1^{\mathsf{T}}, \ldots, \mathbf{A}_{NK}^{\mathsf{T}}]^{\mathsf{T}}$, this allows us to relax (17) as the following semidefinite program (SDP) [38]:

$$\begin{aligned} \max_{\mathcal{C},\lambda} \quad & \lambda \\ \text{s.t.} \quad & \mathbf{A}^{\mathsf{H}}(\mathcal{C}\otimes\mathbf{I}_{FN})\mathbf{A} - \lambda\mathbf{I}_M \succeq \mathbf{0} \\ & \mathcal{C} \succeq \mathbf{0} \\ & \mathbf{1}^{\mathsf{T}}\text{diag}(\mathcal{C}) = 1. \end{aligned} \tag{20}$$

Note that $||\mathbf{c}||_2^2 = 1$ is equivalent to $\mathbf{1}^{\mathsf{T}}\text{diag}(\mathcal{C}) = 1$. The matrix inequality constraint is now linear in $\mathcal{C}$, and thus, the whole problem is convex.

Based on this formulation, we can also modify the problem to a subsampled scenario by defining $\mathbf{z} = \mathbf{A}_{\mathbf{c}}\mathbf{R}\mathbf{s}_r + \mathbf{n}$ where $\mathbf{R} \in \mathbb{R}^{M\times S}$ is a subsampling matrix, S is the number of subsamples and $\mathbf{s}_r$ contains only the pixels from the subsampled area. Note that this scenario ignores the contribution of most of the pixels in the area, and it does not give the optimal solution for the overall area. However, it is applied because of the substantial computational complexity of solving the SDP (20). The subsampled problem formulation is given by:

$$\begin{aligned} \max_{\mathcal{C},\lambda} \quad & \lambda \\ \text{s.t.} \quad & \mathbf{R}^{\mathsf{T}}\mathbf{A}^{\mathsf{H}}(\mathcal{C}\otimes\mathbf{I}_{FN})\mathbf{A}\mathbf{R} - \lambda\mathbf{I}_S \succeq \mathbf{0} \\ & \mathcal{C} \succeq \mathbf{0} \\ & \mathbf{1}^{\mathsf{T}}\text{diag}(\mathcal{C}) = 1. \end{aligned} \tag{21}$$

Note that the size of the first constraint significantly decreases due to subsampling the data.

b) Det-Opt: Second, we can consider minimizing the determinant of the CRB matrix, which is referred to as the Det-Opt criterion. The problem can then be formulated as

$$\begin{aligned} \min_{\mathbf{c}} \quad & \det(\mathbf{F}^{-1}(\mathbf{c})) \\ \text{s.t.} \quad & ||\mathbf{c}||_2^2 = 1. \end{aligned} \tag{22}$$

Since the CRB matrix is the inverse of the Fisher information matrix, (22) is equivalent to

$$\begin{aligned} \max_{\mathbf{c}} \quad & \det(\mathbf{A}_{\mathbf{c}}^{\mathsf{H}}\mathbf{A}_{\mathbf{c}}) \\ \text{s.t.} \quad & ||\mathbf{c}||_2^2 = 1. \end{aligned} \tag{23}$$

Applying the same relaxation techniques and replacing $\det(\mathbf{F}(\mathbf{c}))$ with $\log(\det(\mathbf{F}(\mathbf{c})))$ we obtain the problem

$$\begin{aligned} \max_{\mathcal{C}} \quad & \log(\det(\mathbf{A}^{\mathsf{H}}(\mathcal{C}\otimes\mathbf{I}_{FN})\mathbf{A})) \\ \text{s.t.} \quad & \mathcal{C} \succeq \mathbf{0} \\ & \mathbf{1}^{\mathsf{T}}\text{diag}(\mathcal{C}) = 1. \end{aligned} \tag{24}$$

Since $\log(\det(\mathbf{F}(\mathbf{c})))$ is known to be concave for a positive semidefinite matrix $\mathbf{F}(\mathbf{c})$, the above optimization problem is convex [42].

c) Trace-Opt: Third, we consider minimizing the trace of the CRB matrix, called Trace-Opt, which is given by

$$\begin{aligned} \min_{\mathbf{c}} \quad & \text{trace}(\mathbf{F}^{-1}(\mathbf{c})) \\ \text{s.t.} \quad & ||\mathbf{c}||_2^2 = 1. \end{aligned} \tag{25}$$

By again applying the same convex relaxation techniques, we attain the following minimization problem:

$$\begin{aligned} \min_{\mathcal{C}} \quad & \text{trace}((\mathbf{A}^{\mathsf{H}}(\mathcal{C}\otimes\mathbf{I}_{FN})\mathbf{A})^{-1}) \\ \text{s.t.} \quad & \mathcal{C} \succeq \mathbf{0} \\ & \mathbf{1}^{\mathsf{T}}\text{diag}(\mathcal{C}) = 1. \end{aligned} \tag{26}$$

To eliminate the large inverse term from the objective function, we first reformulate the problem as follows:

$$\begin{aligned} \min_{\mathcal{C},\mathbf{T}} \quad & \text{trace}(\mathbf{T}) \\ \text{s.t.} \quad & \mathbf{T} - (\mathbf{A}^{\mathsf{H}}(\mathcal{C}\otimes\mathbf{I}_{FN})\mathbf{A})^{-1} \succeq \mathbf{0} \\ & \mathcal{C} \succeq \mathbf{0} \\ & \mathbf{1}^{\mathsf{T}}\text{diag}(\mathcal{C}) = 1. \end{aligned} \tag{27}$$

where $\mathbf{T}$ is introduced as the upper bound of the term inside the trace(.). Now, we minimize $\text{trace}(\mathbf{T})$ instead of $\mathbf{A}^{\mathsf{H}}(\mathcal{C}\otimes\mathbf{I}_{FN})\mathbf{A})^{-1}$ [38]. Using the Schur complement method [43], we finally obtain

$$\begin{aligned} \min_{\mathcal{C},\mathbf{T}} \quad & \text{trace}(\mathbf{T}) \\ \text{s.t.} \quad & \begin{bmatrix} \mathbf{T} & \mathbf{I}_M \\ \mathbf{I}_M & \mathbf{A}^{\mathsf{H}}(\mathcal{C}\otimes\mathbf{I}_{FN})\mathbf{A} \end{bmatrix} \succeq \mathbf{0} \\ & \mathcal{C} \succeq \mathbf{0} \\ & \mathbf{1}^{\mathsf{T}}\text{diag}(\mathcal{C}) = 1. \end{aligned} \tag{28}$$

Similar to (21), we can apply subsampling to Det-Opt criterion in (24) and Trace-Opt criterion in (28).

Now, solving (20), (24) or (28) for $\mathcal{C}$ yields the optimized encoding matrix. As the resulting solution $\hat{\mathcal{C}}$ from (20), (24) or (28) is not guaranteed to have rank one, an approximate rank-one solution can be found by choosing the largest eigenvector of $\hat{\mathcal{C}}$. However, the effectiveness of this method depends on the low rankness of $\hat{\mathcal{C}}$. Another widely employed approach is the randomization method, where we treat $\hat{\mathcal{C}}$ as a covariance matrix to generate multiple candidate random vectors from $\hat{\mathbf{c}} \sim \mathcal{N}(0, \hat{\mathcal{C}})$. Subsequently, these solutions are projected onto the original constraint set. In our case, every randomization is normalized here to satisfy the energy constraint. Each candidate is then applied to the original problem (15), (22) or (25), and the realization that optimizes the related cost is selected as the solution [44]. This approach is regularly used in literature thanks to its proven success in many studies and its theoretical performance guarantees for several discrete optimization problems [44], [45]. While we cannot establish a lower bound on the optimality of this method, empirical observations demonstrate that this approach consistently outperforms solutions derived from the leading eigenvector. Note that if $\hat{\mathcal{C}}$ is found to have

rank one, the random vectors generated using $\hat{\mathcal{C}}$ as covariance matrix will be identical to the leading eigenvector of $\hat{\mathcal{C}}$, up to a scalar value.

The previous optimization schemes in (15), (22), or (25) represent the optimal MSE solution. However, due to the substantial pixel count in the imaging area, the computational demands of the cost function become significant. This involves calculating and storing a significant number of $\mathbf{A}_p^{\mathsf{H}}\mathbf{A}_q \in \mathbb{C}^{M\times M}$ matrices, making it computationally challenging and memory-intensive to implement and solve in cvx, which is a MATLAB toolbox for solving convex optimization problems [46]. One way is to optimize the codes for the subsampled imaging area with fewer pixels, such as proposed in (21). However, this solution will be suboptimal as the new CRB for the subsampled data will not be optimal for the overall system. Another way to address this limitation is to explore a suboptimal optimization function that is less complex and more efficient.

B. FIM Maximization

Rather than minimizing the trace of the CRB matrix in (25), an alternative approach involves maximizing the trace of the FIM. An optimized encoding matrix can be obtained by maximizing the Fisher information within a region of interest (ROI). Thanks to the linearity of the trace operator, this proposed approach becomes computationally more efficient than the optimization schemes outlined in (20), (24) or (28). However, it may not achieve the optimal MSE, potentially resulting in a degradation of image quality. This degradation results from the fact that trace-based FIM maximization and trace-based CRB minimization are not mathematically equivalent optimization problems since the trace(.) operator is not linear.

Although this is not equivalent to the minimization problem in (25), we can maximize the trace of the FIM as expressed in (14) which leads to

$$\max_{\mathbf{c}} \quad \text{trace}(\mathbf{A}_{\mathbf{c}}^{\mathsf{H}}\mathbf{A}_{\mathbf{c}}) \qquad \text{s.t.} \quad ||\mathbf{c}||_2^2 = 1. \tag{29}$$

Through the transformation of $\mathbf{A}_{\mathbf{c}}^{\mathsf{H}}\mathbf{A}_{\mathbf{c}}$ using (18), its trace can be written as

$$\begin{aligned}\text{trace}(\mathbf{A}_{\mathbf{c}}^{\mathsf{H}}\mathbf{A}_{\mathbf{c}}) &= \sum_{p=1}^{NK}\sum_{q=1}^{NK} c_p^* c_q \text{trace}(\mathbf{A}_p^{\mathsf{H}}\mathbf{A}_q) \\ &= \mathbf{c}^{\mathsf{H}}\mathcal{A}\mathbf{c},\end{aligned} \tag{30}$$

where $\mathcal{A}$ is given by

$$\mathcal{A} = \begin{bmatrix} \text{trace}(\mathbf{A}_1^{\mathsf{H}}\mathbf{A}_1) & \dots & \text{trace}(\mathbf{A}_1^{\mathsf{H}}\mathbf{A}_{NK}) \\ \vdots & & \vdots \\ \text{trace}(\mathbf{A}_{NK}^{\mathsf{H}}\mathbf{A}_1) & \dots & \text{trace}(\mathbf{A}_{NK}^{\mathsf{H}}\mathbf{A}_{NK}) \end{bmatrix}. \tag{31}$$

As a result, (29) can be simplified as

$$\max_{\mathbf{c}} \quad \mathbf{c}^{\mathsf{H}}\mathcal{A}\mathbf{c} \qquad \text{s.t.} \quad \|\mathbf{c}\|^2 = 1. \tag{32}$$

The solution to this problem is well-known by Lagrange multipliers and is given by the eigenvector of $\mathcal{A}$ corresponding to the largest eigenvalue [47].

Notably, the matrix $\mathcal{A}$ is complex and has complex eigenvectors. However, we need to narrow its focus to amplitude and bi-phase encoding. In other words, the encoding vector $\mathbf{c}$ is constrained to the real domain. By decomposing the cost function in (32) using real and complex parts, it can be expressed as

$$\mathbf{c}^{\mathsf{H}}\mathcal{A}\mathbf{c} = \begin{bmatrix}\text{Re}(\mathbf{c})^{\mathsf{T}} & \text{Im}(\mathbf{c})^{\mathsf{T}}\end{bmatrix} \begin{bmatrix}\text{Re}(\mathcal{A}) & -\text{Im}(\mathcal{A}) \\ \text{Im}(\mathcal{A}) & \text{Re}(\mathcal{A})\end{bmatrix} \begin{bmatrix}\text{Re}(\mathbf{c}) \\ \text{Im}(\mathbf{c})\end{bmatrix}. \tag{33}$$

Since only the real part of $\mathbf{c}$ is considered for amplitude and bi-phase encoding, the imaginary part can be set to zero, i.e., $\text{Im}(\mathbf{c}) = \mathbf{0}$. As a result, (33) can be expressed as

$$\text{Re}(\mathbf{c})^{\mathsf{T}}\text{Re}(\mathcal{A})\text{Re}(\mathbf{c}). \tag{34}$$

The amplitude and bi-phase encoding vector can thus be determined by extracting the leading eigenvector from the real part of the matrix $\mathcal{A}$. We will call this method the FIM-Opt approach.

C. Encoding Matrix Optimization for Multiple Transmissions

For multiple transmissions, L distinct encoding matrices are designed to construct a more accurate compounded ultrasound image. Assuming the pixel intensity $\mathbf{s}$ remains constant across these L transmissions, a signal model for the L transmissions and measurements can be expressed as follows

$$\begin{bmatrix}\mathbf{z}_1 \\ \mathbf{z}_2 \\ \vdots \\ \mathbf{z}_L\end{bmatrix} = \begin{bmatrix}\mathbf{A}_{\mathbf{c}_1} \\ \mathbf{A}_{\mathbf{c}_2} \\ \vdots \\ \mathbf{A}_{\mathbf{c}_L}\end{bmatrix}\mathbf{s} + \begin{bmatrix}\mathbf{n}_1 \\ \mathbf{n}_2 \\ \vdots \\ \mathbf{n}_L\end{bmatrix}. \tag{35}$$

It is important to note that the model (35) remains linear concerning both $\mathbf{s}$ and the encoding matrices $\mathbf{C}_l$. Consequently, the optimization methods detailed in Sections III-A and III-B can again be employed to address and solve the code design for this model.

Solving for the encoding matrices in (35) using the optimization methods (20), (24) or (28) described in Section III-A would still encounter memory issues when implemented due to the large number of pixels. Alternatively, for the solution based on the minimization of the CRB, we can use the same method as before but adopt the randomization method in the subsampled scenario to obtain L distinct encoding matrices instead of creating the formulation based on (35). We first generate many random vectors from the distribution $\hat{\mathbf{c}} \sim \mathcal{N}(0, \hat{\mathcal{C}})$. Then, we apply them to the original problem and choose L candidates that give the minimum value for (15), (22), or (25). Hence, we find L solutions that minimize the CRB, and these L transmissions are coherently compounded. For the solution based on the maximization of the FIM, it is observed that multiple large eigenvalues of $\mathcal{A}$ are close to each other, suggesting the presence of multiple suboptimal solutions. Therefore, a potential solution could involve the first few leading eigenvectors corresponding to these largest eigenvalues for multiple transmissions. Then, each eigenvector is normalized and selected as a coding vector of each transmission, and finally, these L transmissions are compounded.

D. Computational Complexity

The FIM-Opt approach requires the computation of the $\mathcal{A}$ matrix in (31). Because of the trace operator, this requires calculating the diagonal of $N^2\,K^2$ matrices of the form $\mathbf{A}_p^{\mathsf{H}}\mathbf{A}_q \in \mathbb{C}^{M\times M}$ (see (19); for the subsampled scenario, we can simply change M by S). Computing the diagonal of each $\mathbf{A}_p^{\mathsf{H}}\mathbf{A}_q$ requires a complexity of $\mathcal{O}(MFN)$ and the overall cost becomes $\mathcal{O}(N^3\,K^2\,MF)$. Taking the traces of all terms in (31) has complexity $\mathcal{O}(N^2\,K^2\,M)$; which is relatively negligible. Later, computing the eigenvectors of the resulting $\mathcal{A}$ matrix brings a computational complexity of $\mathcal{O}(N^3\,K^3)$, which is again negligible. Note that N in our case is of size 80 or 128 and $2 \leq K \leq 5$. Hence, the optimization procedure with FIM-Opt has an overall computational complexity of $\mathcal{O}(N^3\,K^2\,MF)$.

In Eig-Opt, Dep-Opt and Trace-Opt scenarios, calculating the $N^2\,K^2$ entries of the $\mathbf{A}_p^{\mathsf{H}}\mathbf{A}_q \in \mathbb{C}^{M\times M}$ matrices in (19) has a computational complexity of $\mathcal{O}(N^3\,K^2\,M^2F)$ which is already M times the complexity of the FIM-Opt scenario. Moreover, the computational complexity of the SDP given in (20) or (28) has a complexity of $\mathcal{O}(N^4\,K^2F^2\,M + M^2\,N^2KF)$ per iteration because $\mathbf{A}^{\mathsf{H}}(\mathcal{C}\otimes\mathbf{I}_{FN})\mathbf{A}$ is computed in every iteration with respect to updated codes in SDP. Note that instead of actually implementing the Kronecker product, an equivalent expression in (19) is used. Then, the computational complexity of the SDP per iteration becomes $\mathcal{O}(N^3\,K^2\,M^2F)$. Besides, the cost of the first and second positive semidefinite constraints are $\mathcal{O}(M^3)$ and $\mathcal{O}(N^3\,K^3)$, respectively, in (20) and (28). Since these terms are generally negligible, the overall computational cost of Eig-Opt or Trace-Opt becomes $\mathcal{O}(N^3\,K^2\,M^2FI)$ where I is given by the number of iterations in the SDP solver. Note that cvx uses interior point methods, where each iteration has additional costs, increasing the computation time even further.

While FIM-Opt requires a single step with the complexity of $\mathcal{O}(N^3\,K^2\,MF)$, Eig-Opt, Trace-Opt, and Det-Opt require a notably higher cost, which makes FIM-Opt more useful in practical scenarios. Furthermore, $\mathcal{O}(N^3\,K^2\,M^2FI)$ quadratically increases by M, and the number of pixels can be significantly high in ultrasound imaging, which requires subsampling. Nonetheless, the optimization of the codes is performed only once and can be used in imaging tasks repeatedly.

Finally, the computational cost of matched filtering after the optimization procedure is $\mathcal{O}(MFN)$, which is equivalent for all coding schemes of comparison.

IV. Numerical Results

Simulation experiments are conducted using the k-Wave toolbox [48]. In all k-Wave simulated measurements, the attenuation coefficient has a frequency-dependent power law model for realistic nonlinear ultrasound wave propagation in biological soft tissue. The attenuation is defined as $\alpha(f) = \alpha_0 f^y$ where $\alpha_0 = 0.75$ dB/(MHz$^y\cdot$ cm) is the attenuation coefficient and $y = 1.5$ is the power law exponent.

Two scenarios are considered to evaluate the performance of the proposed optimized code. The first scenario presented in Section IV-A involves a densely sampled high-frequency array with an element pitch-to-wavelength ratio less than 0.5. The second scenario in Section IV-B aims to test the optimized code on a numerical model of the clinical transducer array again with an element pitch-to-wavelength ratio less than 0.5. We used both a high-frequency array and a lower-frequency clinical probe to test our method's robustness across different transducer simulations. Note that high-frequency arrays offer a better resolution for detailed analysis in superficial imaging [49], while low-frequency arrays are useful in practical deep imaging scenarios [1], [2]. In a densely sampled high-frequency array with 128 elements, we first start with a toy example (a simplified simulation) to compare the proposed algorithm with the state-of-the-art. Then, we compare the performance of CRB minimization and FIM maximization for point scatterers data for a highly subsampled optimization scheme. Lastly, the computationally efficient FIM method is chosen to compare its performance with the state-of-the-art. These comparisons are also carried out with the simulated clinical transducer for both point scatterers data and a simulated flow phantom in Doppler imaging.

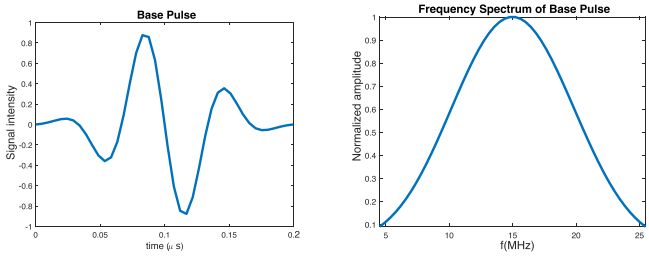

(a) (b)

Fig. 1. Transmit pulse shape: (a) single short pulse (base pulse), (b) frequency spectrum of base pulse.

First, the transmitted pulse length $t_{pulse} \leq 5.19$ μs was chosen to limit the dead-zone to 4 mm. Second, the total pulse length is the length of the base pulse multiplied by the number of bits since we do not consider any overlap between consecutive pulses. In other words, the delay τ between two base pulses is considered equal to the base pulse length. Third, the number of transmissions L is important for the imaging quality. For the initial toy example, we pick $L = 1$ in Section IV-A1. For the cases in Section IV-A2, we select various values of $L = 1, 3, 5, 10$ for comprehensive analysis between CRB minimization and FIM maximization. In ultrafast compounded Doppler imaging, it is experimentally validated that when L reaches 9, the resulting contrast and SNR are satisfying, and image contrast will only slightly improve for $L > 16$ assuming plane-wave imaging [3]. Hence, L bounded between 10 and 16 should be sufficient in literature. Hence, we pick $L = 10$ for the comparisons with the state-of-the-art in Sections IV-A3 and IV-B. Hence, we make sure that all the compared methods are tested with a sufficient number of transmissions. Those methods involve Barker coding, random coding, and plane-wave transmissions.

A. Densely Sampled High-Frequency Array

The densely sampled high-frequency array consists of 128 elements spaced with 25 μm pitch. The ultrasound transducer emits a base pulse with a center frequency of 15 MHz. The base pulse and its frequency spectrum are given in Fig. 1. The imaging region of interest extends from 4 mm to 11 mm in depth

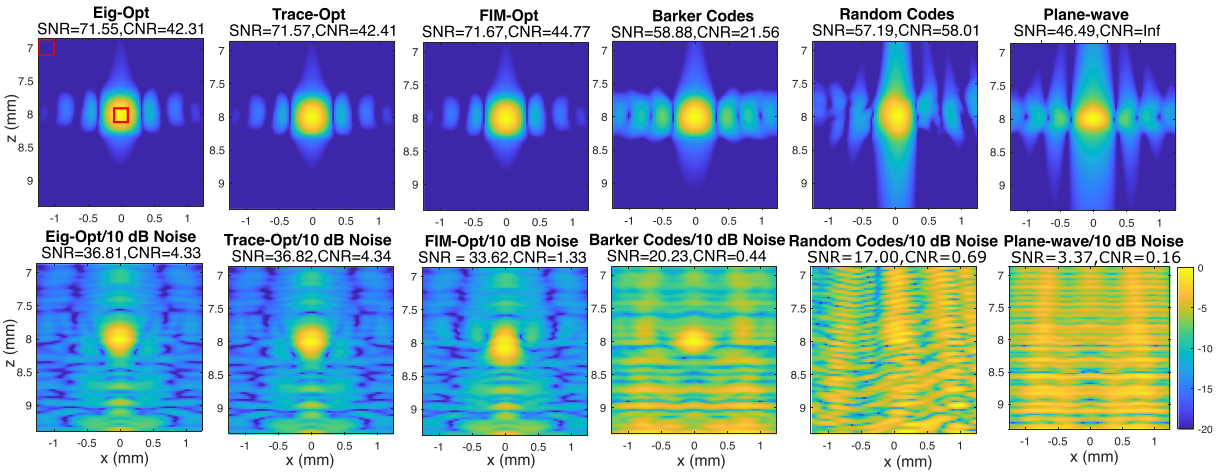

Fig. 2. The single transmission imaging results for optimized transmissions with Eig-Opt, Trace-Opt, FIM-Opt, Barker code, random code, and plane-wave transmission for noiseless data (top) and noisy data with 10 dB SNR (bottom).

and from -1.25 mm to 1.225 mm in width, aligning with the area typically studied in mouse brain imaging. The interpixel spacing is picked as $dz = dx = 25$ µm.

1) Toy Example: In this section, we compare the results of the approaches that rely on the minimization of the CRB and the maximization of the FIM with the state-of-the-art for a single scatterer. For the former approach, we solve the problem given in (20) and (28) using cvx software [46]. However, due to the high computational complexity of the problem, we only focus on a small optimization area with a single pixel. For the latter approach, the solution is given by the leading eigenvector of $\mathrm{Re}(\mathcal{A})$.

Due to the high computational complexity of the CRB-based solution, an optimized encoding matrix of size 128×2 is designed, with the pulse having a short bit-length of 2. To evaluate the performance of the algorithms, we first consider a single scatterer image where the codes are optimized with respect to the known scatterer point, which is located at $[x, y] = [0, 8]$ mm. Since we test only for a single scatterer, such an optimization scheme is sufficient. Ideally, for a larger area of distributed scatterers, the optimization should be performed on the pixels taken from the entire area to improve the SNR performance. Here, we only consider a single transmission, i.e., $L = 1$. We use random rounding for the CRB minimization method, and the single realization that maximizes (20) (Eig-Opt) or minimizes (28) (Trace-Opt) is picked among 100 random vectors that belong to the following distribution $\hat{\mathbf{c}} \sim \mathcal{N}(0, \hat{\mathcal{C}})$. Here, further increasing the number of random vectors did not visibly affect the performance. For the solution based on the maximization of the FIM (FIM-Opt), the leading eigenvector of $\mathrm{Re}(\mathcal{A})$ is selected for transmission. The performance of the methods is compared to the Barker code, random code, and plane-wave transmission under noiseless and noisy conditions with 10 dB SNR. Before transmission, all pulses undergo normalization to ensure uniform average energy levels. Except for the plane-wave transmission, all transmission codes have a length of 2. All results obtained with matched filtering in (12) for these six scenarios are shown in Fig. 2.

The results are numerically analyzed by comparing the SNR and CNR in the four scenarios, where $\mathrm{SNR} = 10\log_{10}(\frac{P_s}{P_n})$. P_s and P_n are the average power of the point scatterer and background noise, respectively. In noise-free cases, P_n corresponds to the average power of the low-intensity background region across the image. Here, $CNR = 10\log_{10}(|\frac{\mu_s - \mu_n}{\sigma_n}|)$ where μ_s and μ_n are mean values of the intensities of point scatterer and background regions, and σ_n is the standard deviation of the noise. To compute the SNR and CNR, the red rectangles are used for the scatterer and background noise. Eig-Opt, Trace-Opt, and FIM-Opt perform similarly in noiseless and noisy cases with 10 dB SNR noise, outperforming the plane-wave, random code, and Barker code reconstructions. Since the formulations in (21) and (28) are the same for the single pixel scenario, it is expected that we observe that both Eig-Opt and Trace-Opt results in the same reconstructions. We also observe that in the noisy case, while Eig-Opt, Trace-Opt, FIM-Opt, and the Barker code approach could reconstruct the scatterer, the other methods could not provide a proper view of the scatterer. The Eig-Opt, Trace-Opt and FIM-Opt results outperform the Barker code in the noisy case. Thanks to the computational efficiency of the FIM-Opt approach, it is more advantageous than both Eig-Opt and Trace-Opt methods.

2) CRB Minimization Versus FIM Maximization: Now, instead of a single scatterer, we consider uniformly distributed point scatterers in Fig. 3. The scatterers are placed 0.625 mm apart both in z and x directions. We compare the imaging performance of three transmission methods: Eig-Opt, Trace-Opt, and FIM-Opt, using 2-bit codes. However, due to the high computational complexity of the problem, we only focus on a small optimization area with few pixels (9 or 121pixels). Since we optimize the codes for a small area, comparing them with the state-of-the-art would be unfair. It was fair for the single scatterer as the codes are optimized with respect to the specific location of the scatterer. Now, the optimization area is significantly smaller than the extent of the uniformly distributed scatterers, and the subset of pixels selected does not overlap with the scatterers. Therefore, only the proposed methods are compared to choose

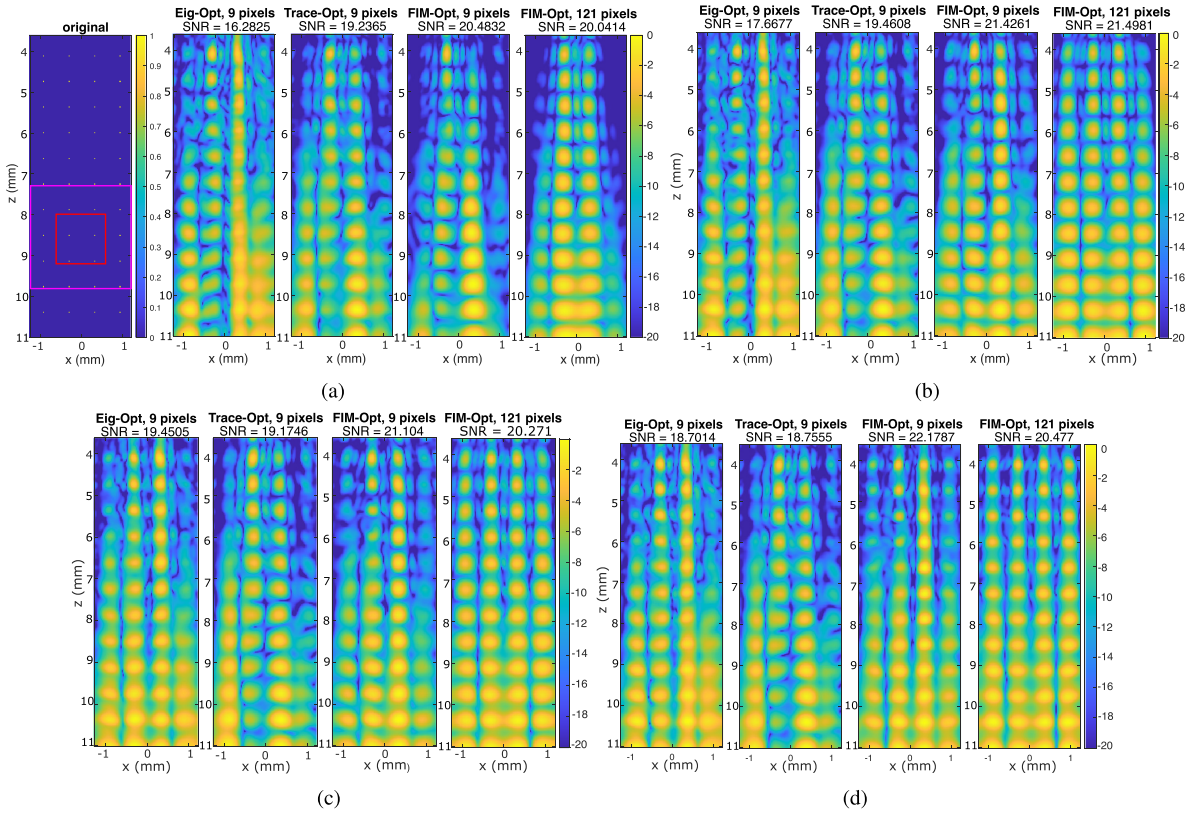

Fig. 3. Simulated imaging performance for densely sampled high-frequency array. The compounded image results for optimized transmissions with Eig-Opt, Trace-Opt, and FIM-Opt using 9 and 121 pixels for (a) single transmission, (b) 3 transmissions, (c) 5 transmissions, and (d) 10 transmissions.

the best one for more comparisons in the next section. Before transmission, all codes undergo normalization to ensure uniform average energy levels.

An image subset of $3 \times 3 = 9$ equidistantly distributed pixels from 8 to 9.3 mm on the z-axis and from -0.65 to 0.65 mm on the x-axis in Fig. 3(a) was chosen for optimization. Note that this area is shown with a red rectangle where the scatterers and selected pixels do not overlap. This area is chosen in the middle of the region of interest between 6 mm to 11 mm. Such a low number of pixels is selected due to the computational complexity of the semidefinite program in (20) for Eig-Opt and (28) for Tra-Opt, which is solved via the cvx toolbox. On a Dell server with dual AMD EPYC 7551 processors (64 cores total, 128 threads, 128GB RAM, 1TB SSD), optimization with Eig-Opt takes approximately 1800 seconds, Tra-Opt takes about 2600 seconds, and FIM-Opt completes in around 20 seconds for 9 pixels. While this server is optimized for fast computation, running the same algorithms on a standard MacBook Pro 2019 (2.6GHz 6-core Intel Core i7) takes roughly 10,000 seconds for Eig-Opt and Tra-Opt. The middle three plots in Fig. 3(a) and the first three plots in Fig. 3(b), (c) and (d) are obtained with the optimized code that relies on 9 pixels. Hence, we compare the results for minimizing the CRB based on the Eig-Opt and Trace-Opt criterion and maximizing the FIM for the same pixels.

In the second scenario, a subset of pixels comprising $11 \times 11 = 121$ equidistantly distributed pixels spanning from 7.3 to 9.9 mm on the z-axis and from -1.3 to 1.3 mm on the x-axis in Fig. 3(a) was chosen to maximize the FIM where the area is shown with a magenta rectangle. Although there is not a specific reason for the exact choice of 11×11, we aim to exceed the performance of the CRB minimization for a small area (9pixels) by maximizing the FIM for a larger area (121 pixels), with lower computational complexity. Indeed, it is significantly lower as it only takes around 160 seconds with the given Dell server. However, Eig-Opt and Tra-Opt algorithms exceed 36 hours for 121 pixels scenario; hence, it is not practical. The last plots are obtained with the optimized code concerning 121 pixels in Fig. 3. Note that the computational cost of FIM-Opt, even with more pixels, is still lower than the Eig-Opt and Trace-Opt methods.

For each method $L = 1$, $L = 3$, $L = 5$ and $L = 10$ transmissions are compounded. These codes are generated randomly for the Eig-Opt and Trace-Opt which employ the mentioned random rounding method in Section III-C, and L realizations that minimize (15) or (25) are picked, respectively. With FIM-Opt, the leading L eigenvectors of $\mathrm{Re}(\mathcal{A})$ are selected for transmission. All results obtained with matched filtering from $L = 1$, $L = 3$, $L = 5$, and $L = 10$ transmissions for these four scenarios are shown in Fig. 3. We only show the results without noise in Fig. 3. Moreover, Fig. 4 shows individual transmissions of the Eig-Opt algorithm compounded in Fig. 3(c). Here, each transmission focuses on a different part of the image, hence showing the necessity of various transmissions. The SNR values given in Fig. 3 are obtained by taking the average power of all the known scatterer locations for P_s. To compute P_n, noise locations are selected at the central points between every four scatterers, where the scatterers form the corners of a rectangle. These central

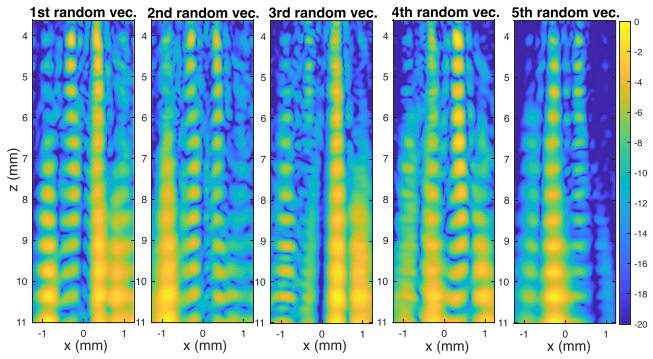

Fig. 4. Simulated imaging performance for the densely sampled high-frequency array with the imaging results of $L = 5$ transmissions for Eig-Opt.

points represent regions expected to contain minimal signal, primarily dominated by noise. Across the reconstructions, single transmission is insufficient for a good reconstruction quality for all methods, as shown in Fig. 3. The resolution of the scatterers increases with $L = 5$ transmissions especially for FIM-Opt method and the entire ROI even becomes more resolvable with $L = 10$ transmissions. In terms of the clarity of all scatterers, the Eig-Opt performs similarly to the FIM-Opt, where the performance of Trace-Opt seems to be slightly weaker than the others. FIM-Opt outperforms both Eig-Opt and Trace-Opt in terms of SNR. When the region of interest for maximizing the FIM is extended from 9pixels to 121pixels, the scatterers in the entire ROI become more resolvable. In contrast, the SNR values for FIM-Opt for 9pixels seem higher. This is due to scatterers in the middle of the x -axis seeming to be very bright and increasing the average SNR for FIM-Opt with 9pixels. Here FIM-Opt optimized based on 121pixels and with 10 transmissions seems to provide a good balance between resolution and SNR by capturing the entire area of scatterers.

The computational complexity of the CRB minimization is significantly higher than the FIM maximization, and hence, FIM-Opt is more advantageous than others also in terms of computational cost. While the Eig-Opt and Trace-Opt require solving a high-cost SDP given in (20) or (28) using a toolbox such as cvx, the FIM-Opt only takes L eigenvectors of $\mathrm{Re}(\mathcal{A})$ in (31). In the FIM-Opt method, irrespective of the area of interest, the size of the $\mathcal{A}$ matrix in (31) is the same for the same code length and number of transmitters. The only increment in the computational complexity is calculating the $\mathcal{A}$ matrix. In the end, FIM-Opt is exploited for the rest of the simulations thanks to its reconstruction quality and computational efficiency.

3) FIM Maximization Versus the State-of-the-Art: In this section, an optimized encoding matrix of size 128×5 is designed, with the pulse having a bit-length of $K = 5$. We compare the imaging performance of four transmission methods: single short pulse plane-wave, 5-bit Barker code, 5-bit random code, and 5-bit optimized code with FIM-Opt. Before transmission, all codes are normalized to ensure uniform average energy levels. Here, images from $L = 10$ transmissions are compounded. The scatterers are placed 0.625 mm apart in the z direction and 0.45 mm apart in the x direction, respectively. For FIM-Opt, an image subset between 6 to 11 mm in the z-axis and between -1.5 mm to 1.5 mm in the x-axis was chosen for optimization,

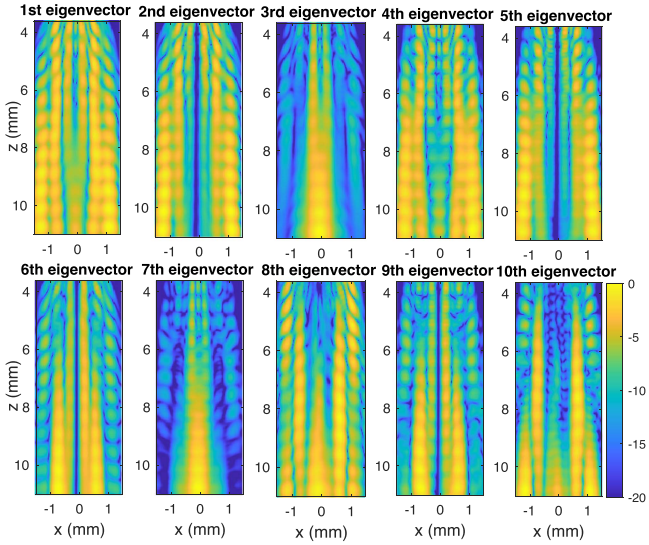

Fig. 5. Simulated imaging performance for a probe geometry matching that of a densely sampled high-frequency array based on the 10 leading eigenvectors with FIM-Opt Method.

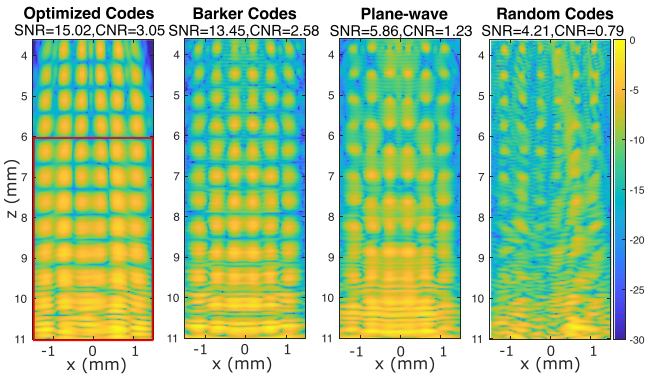

Fig. 6. Simulated imaging performance for densely sampled high-frequency array for optimized code, Barker code, plane-wave, and random transmission with SNR = 10 dB.

as shown with the red rectangle in Fig. 6. This image subset contains $50 \times 30 = 1500$ equidistantly distributed pixels. The distance between each pixel used for optimization is 0.1 mm in the z and x directions, four times the interpixel distance. Since the construction of $\mathcal{A}$ takes time when the area is extended, the optimization region is limited.

Fig. 5 shows the matched filter imaging results from the optimized (FIM-Opt) code based on the 10 leading eigenvectors. It shows that each eigenvector transmission produces a different focusing area in the image, leading to varying imaging results. This finding highlights the need for different optimized encoding matrices for multiple transmissions. Then, the compounded imaging results are shown in Fig. 6 for all methods. These are reconstructed from measurements with the same additive white Gaussian complex noise at SNR of 10 dB. The left-most image is obtained with the optimized code by compounding data from the 10 leading eigenvectors. The subsequent two images display results from Barker-5 transmissions and single pulse plane-wave transmissions by compounding the data from 10

TABLE I
AXIAL AND LATERAL FWHM OF PSF

FWHM (mm)	Optimized	Barker	PW	Random
Axial	0.423	0.342	0.327	0.266
Lateral	0.333	0.323	0.310	0.262

insonified angles spanning $[-12°, 12°]$. Meanwhile, the fourth image is acquired and compounded through 10 instances of 5-bit random code transmissions.

The SNR values in Fig. 6 are obtained by taking the average power of all the known scatterer locations as P_s and picking a low-intensity point between every four scatterers for P_n, where the scatterers form the corners of a rectangle. Although the optimization of the codes is performed for an area smaller than the ROI, the SNR values are acquired with the points picked from the entire ROI. The CNR values are also attained in a similar fashion. The results show that the optimized transmission produces the highest SNR and CNR, and the reconstructions appear brighter in the deeper area ranging from 7 to 9 mm. Conversely, the Barker code and plane-wave transmissions show distortions starting from approximately 8 mm depth. Distortions are also present for the optimized codes, but their effect is less severe thanks to the higher SNR of optimized codes. Lastly, a random transmission appears to be the most sensitive to additive noise, leading to significant degradation in image quality. In summary, Barker codes outperform plane-wave and random codes in the deeper region but still fall short compared to the optimized transmission regarding SNR and noise sensitivity.

To measure resolution, we used the full width at half maximum (FWHM) of the point spread function (PSF) at the scatterer locations. The FWHM represents the width of the PSF at 50% of its peak value and indicates how well nearby points can be distinguished. We report both axial and lateral FWHM values as indicators of spatial resolution. The FWHM of the PSF for resolution is given in Table I for the images in Fig. 6. The twelve scatterers inside the region over the [6,7.5] mm across z-axis have been used and their FWHM values are averaged. These scatterers are chosen as they are in the optimization area, and they do not suffer from the degradations starting around 8 mm for random codes. The optimized codes present the worst resolution and the highest FWHM value. Then, Barker codes and plane-wave produce better axial and lateral resolution, and random codes result in the best resolution values.

A trade-off between SNR and resolution (both axial and lateral) for the optimized code is observed. This trade-off arises from the limitation in the optimization formulation (32), where the autocorrelation property of the code is not considered. The autocorrelation function (ACF) of the optimized code (on the 80th element) and the 5-bit Barker code is plotted in Fig. 7. It can be seen that the normalized main lobe amplitude (the highest peak) of the optimized code (0.55) is higher than the Barker code (0.25) by a factor of 2. However, the main lobe-to-side lobe (the second highest peak) ratio of the optimized code 1.89 is considerably lower than that of the Barker code (5). A lower main lobe-to-side lobe ratio increases interference and artifacts caused by side lobe energy and results in smoother images with worse resolution. Although a high main lobe level can result in a higher SNR in the image; a low main lobe-to-side lobe ratio causes a degraded resolution for optimized codes.

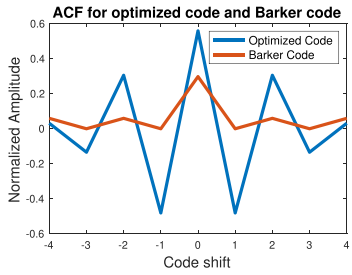

Fig. 7. Normalized autocorrelation function for optimized code on the 80th element, $[0.75, -1.58, 1.88, -1.51, 0.70]$, and Barker code of length 5, $[1, 1, 1, -1, 1]$. These codes are scaled with the same factor after normalization to show the magnitude of the optimized codes compared to standard Barker codes.

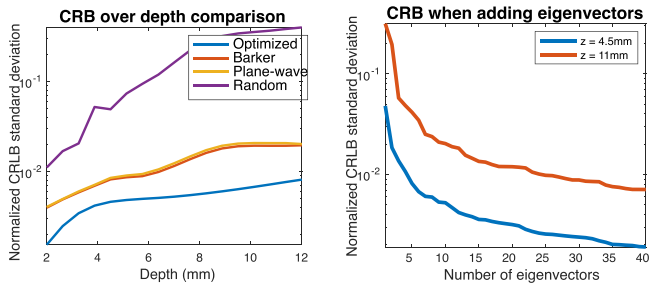

(a) (b)

Fig. 8. (a) CRB versus depth for random, Barker, plane-wave, and optimized code at -0.7 mm on x-axis; (b) CRB versus L, the number of compounded eigenvectors, for a pixel at depth 4.5 mm and depth 11 mm.

We evaluate the CRB of the four methods across different imaging depths, as shown in Fig. 8(a). The results reveal that the FIM-Opt code yields the lowest CRB, indicating superior estimation precision of optimized codes, meaning it provides the most accurate estimation of scatterer intensities among the tested methods. Meanwhile, the Barker code and short pulse plane-wave exhibit similar CRB curves and the random code displays the highest CRB values. These SNR values align with the trends observed in the imaging results. Hence, this analysis confirms the effectiveness of the FIM-Opt code compared to the other tested methods in terms of increased SNR.

Remark 1: Note that number of transmissions L can also be analyzed from the CRB perspective. Thus, how the CRB changes when compounding more leading eigenvectors for multiple transmissions is investigated. In Fig. 8(b), the normalized CRB is plotted for a pixel located at depths of 4.5 mm and 11 mm when compounding 1 to 40 leading eigenvectors. It becomes evident that after compounding 5 transmissions, the CRB no longer decreases significantly. Still, to accommodate the literature, the number of transmissions L is set to 10 for good compounded image quality.

B. Simulated Clinical Transducer Results

Here, the M5Sc-D phased array transducer manufactured by General Electric (GE) with its 80×3 elements and a pitch of 0.27 mm is used. This transducer complies with the Nyquist sampling requirement, operating at a center frequency of 2.8 MHz with wavelength $\lambda = 0.55$ mm. We only consider using the

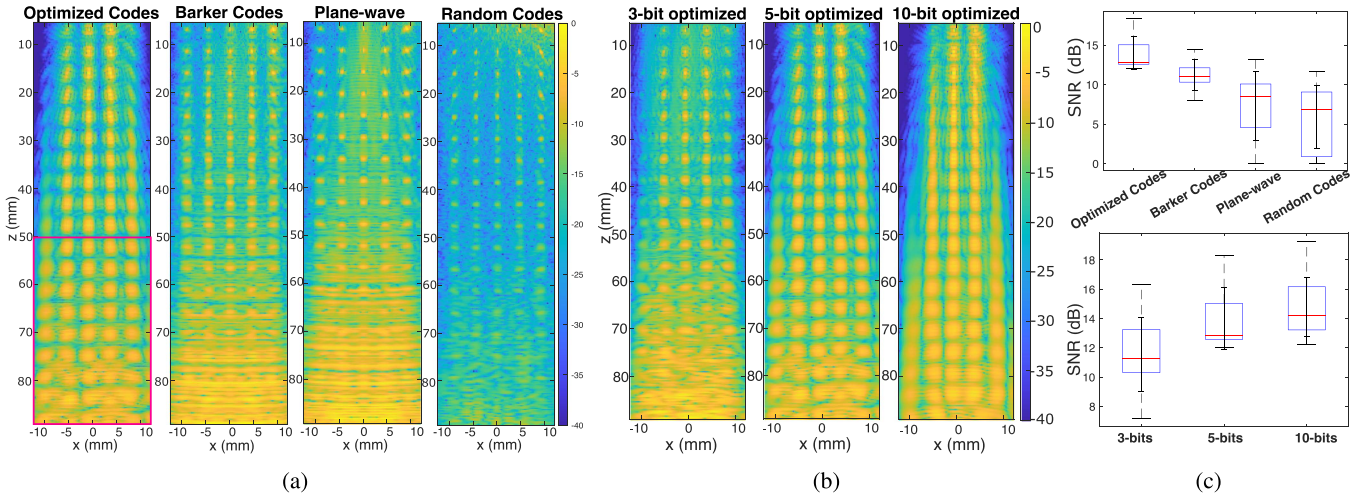

Fig. 9. Simulated imaging performance for a probe geometry matching that of a clinical transducer (a) Imaging results for optimized code, Barker codes, plane-wave, and random transmissions with SNR $= 10$ dB. (b) Imaging results for 3-bit, 5-bit, and 10-bit optimized codes with SNR $= 10$ dB. (c) The SNR boxplot analysis for point scatterer images with optimized codes, Barker codes, single pulse plane-wave, and random codes (top) and with 3-bit, 5-bit, and 10-bit optimized codes(bottom). In each box, the bottom and top edges of the box represent the 25th and 75th percentiles in the data, and the red line inside the box marks the median. The whiskers represent the highest and lowest values in the data.

middle row elements, resulting in 80 active elements. The choice was made for computational efficiency, as it reduces the number of elements. Although this limits the shape of the beam in the elevation direction, it allows for a focused investigation of beamforming performance in the lateral direction. The pixel spacing is $dz = dx = 90$ µm.

1) Matched Filter Results: Simulations are conducted using equidistantly distributed point scatterers within the imaging area. The encoding matrix $\mathbf{C}$ was optimized with dimensions 80×5, focusing on an image subset ranging from around 50 mm to 90 mm in the z-axis and -12 mm to 12 mm in the x-axis which is shown with the red rectangle in Fig. 9(a). This image subset contains $90 \times 44 = 3960$ equidistantly distributed pixels. Here, the distance between each pixel used for the optimization is 0.54 mm in the z and x directions, 6 times the interpixel distance. Its performance was compared to the 5-bit Barker code, single pulse plane-wave, and 5-bit random code. The imaging region ranges from 5 mm to 90 mm. Fig. 9(a) displays the results obtained from compounding 10 transmissions, all subject to the same level of additive white Gaussian noise (SNR $= 10$ dB).

In Fig. 9(a), the imaging result beginning at 55 mm with the optimized code is more detectable and more robust to the noise than the Barker code, the plane-wave, and random codes in the deeper regions. Note that the proposed coding scheme is optimized for the area between 50 mm and 90 mm. Therefore, the performance enhancement is expected in that area. As a trade-off, the optimized code has a lower resolution than the other alternatives. Another trade-off of the optimized code is that it results in a narrower field of view compared to other methods. The top left and right point scatterers are not detectable since the near field between 5 mm to 50 mm is ignored for optimization, and some information loss may exist in the near field area. Among other methods, the 5-bit Barker code seems to have higher SNR than the other but slightly degrades the axial resolution compared to the plane-wave or random codes, leading to visible side lobes at point targets as the Barker code does not possess perfect side lobe cancellation after pulse compression [32]. To quantify this, a vertical line at $x = [-0.6875]$ mm is analyzed. Along the axial direction, 19 scatterers are considered to compute the average main lobe-to-side lobe ratio, which is found to be 8.46 dB. The optimized code performs even worse in this regard, yielding a lower ratio of 3.38 dB. Conversely, the random code exhibits better axial resolution than the other methods, particularly in the near-field area [26]. However, the SNR of the random code is notably lower than other methods. In conclusion, the trade-off between the SNR of the optimized code and axial resolution is also observed in Fig. 9(a).

The results are numerically analyzed by comparing the SNR in the four scenarios. For this calculation, a line at $x = [-0.6875]$ mm is picked. We aim to give the reader a richer view of what is happening with the SNR at various depths. The middle line is chosen as the limited optimization region affects the field of view in the corners. Boundary effects have less influence on the middle. This region is where the optimization is most effective, providing a more reliable and representative evaluation of the method. The highest-intensity and lowest-intensity regions are determined on this line. It results in 19 high-intensity regions, corresponding to approximate locations of 19 point scatterers at $x = [-0.6875]$ mm. Then 19 lowest intensity regions in this line are selected and considered as background noise. Each SNR value is computed between a high-intensity region and neighboring a low-intensity region and results in 19 SNR values. Using these 19 SNR values, the box plots of the SNR data from each method are shown in Fig. 9(c). The optimized code has the highest SNR among all methods. A single pulse plane-wave has the highest variation. If we look at the median SNR value, the optimized code has an SNR gain of 4.4 dB, while the Barker code has a gain of 2.5 dB compared to the single short pulse. Note that the optimized and Barker codes maintain a more consistent SNR performance than single pulse and random code.

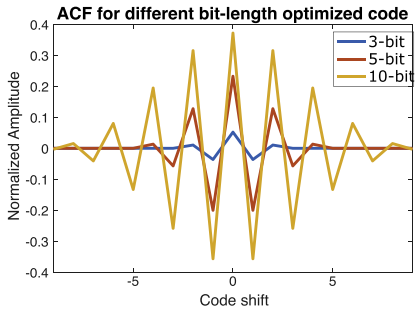

Fig. 10. Autocorrelation function for 3-bit, 5-bit, and 10-bit optimized codes.

Furthermore, the performance of different bit-length optimized codes (3-bit, 5-bit, and 10-bit) is compared. The results are shown in Fig. 9(b) and (c). As the bit-length increases, the SNR also increases. Note that longer codes have higher main lobe levels after pulse compression, resulting in a stronger signal relative to the noise, especially in the deeper regions. However, the use of longer codes also involves a trade-off. Specifically, a 10-bit code exhibits lower resolution for point scatterers compared to the 3-bit and 5-bit codes. As can be seen from the autocorrelation function of optimized codes in Fig. 10, the 10-bit code has the highest main lobe amplitude but the lowest main lobe to side lobe ratio which is only 1.19. The 3-bit code has the lowest main lobe level but has a main lobe-to-side lobe ratio of 5, which is equal to the 5-bit Barker code.

2) LSQR Results: Instead of reconstructing the image with the matched filter, we can also seek a better fit between the data and the model by applying LSQR to improve the resolution of the optimized code results. Experiments with the number of iterations from 1 to 16 were conducted. Fig. 11(a) displays images obtained at different iteration steps. The optimized code results show that the image resolution improves as the number of iterations increases. However, after around 10 iterations, the image starts to overfit with the noise. Especially in deeper areas with lower signal levels, it leads to a decrease in the SNR and overall image quality. We observed this effect visually in the reconstructed images, where noise patterns become more prominent. Furthermore, the point scatterers at two sides at the top of the image become visible within the increasing number of iterations, which were not clear in matched filter reconstructions in Fig. 9(a) with optimized code.

The LSQR results from the optimized code are compared to those from the Barker code, as shown in Fig. 11(b). The results indicate that LSQR does not significantly improve the SNR for the Barker code. Although the resolution improves slightly with an increase in the number of iterations, the near-field area starts to overfit with the noise after 7 iterations. Analyzing the normalized residual curve for these two coded excitation schemes reveals that the residual does not decrease significantly for Barker codes compared to optimized codes with the addition of more iterations (Fig. 12).

In a direct comparison of the best performance image using LSQR between these two transmission schemes (e.g., the 10th iteration for optimized codes and the 7th iteration for Barker codes), the optimized codes still outperform Barker codes in terms of SNR in deeper areas while achieving a decent

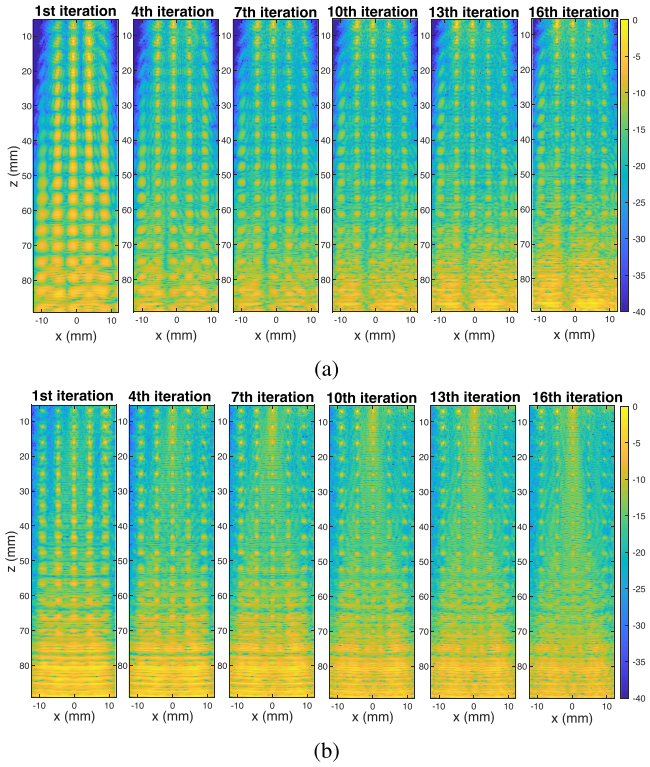

Fig. 11. Simulated imaging performance for a probe geometry matching that of a clinical transducer for (a) Optimized code using Least Squares QR (LSQR) algorithm (b) Barker code using LSQR algorithm. Here, we show the images after 1 to 16 iterations.

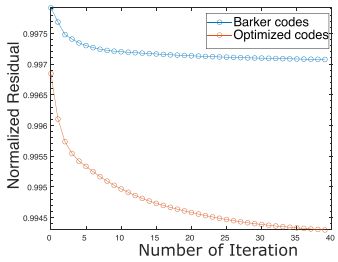

Fig. 12. Normalized residual curves for Barker code and optimized code when adding iteration in LSQR.

resolution. Fig. 13 shows the contrast signal for a vertical line located at position 0.24 mm on x-axis in the image. The scatterers show clear peaks before 60 mm for both methods. The Barker code starts to fail in the area deeper than 60 mm, while the optimized code still maintains a good contrast.

C. Doppler Flow Simulations

In this section, the blood flow imaging simulation is done in k-Wave using MATLAB. The clinical transducer setting described in Section IV-B is used here. A flow phantom with a size of 90 $\times$ 20 mm is generated with a 9 mm diameter parabolic blood vessel that is placed 55 mm away and angled at 25° from the transducer surface. The flow velocity is 9 cm/s, and the blood-to-tissue level is -67 dB. The simulated number of frames is 30. The tissue density is modeled as a random distribution

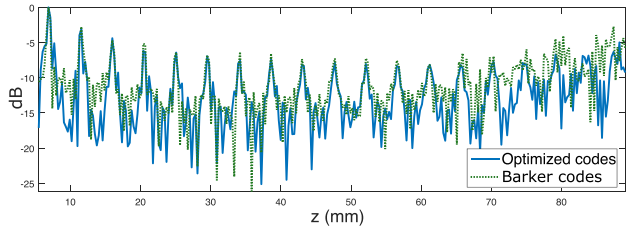

Fig. 13. Image contrast of a vertical line from the image at 0.24 mm on x-axis to noise comparison between optimized code at 10th and Barker code at 4th iteration.

with a mean value of approximately 1000 $\mathrm{kg/m^3}$. The scatterer density in the blood vessel region is also randomly distributed with values ranging from 1000 $\mathrm{kg/m^3}$ to 1020 $\mathrm{kg/m^3}$, where the vessel wall is assumed static. The imaging performance of the 5-bit optimized code and 5-bit Barker code is compared for 10 transmissions. The matched filter is used for beamforming, and after compounding, an SVD filter is applied to all the temporal compounded images to gain the final power Doppler image [12].

Different levels of white Gaussian noise at the noise-to-blood level of -30, -15, and 0 dB are added to the measurement data. The results are shown in Fig. 14. The SNR and the contrast-to-noise ratio (CNR) are calculated for each image, where the blood vessel area and the tissue area are indicated by the black and white rectangular in Fig. 14 respectively. These regions are selected considering the actual locations of the blood vessel and the tissue area in the simulated flow image. We aimed to observe the effect of different codes around the boundaries of the blood vessel. After SVD filtering, the PDI results at a noise level of 0 and -15 dB show that the blood vessel images from the optimized code exhibit a better distinction between vessel and background regions and have stronger intensity compared to the ones from the Barker code (Fig. 14). In the deeper area (below 60 mm), the optimized code exhibits an improved contrast between the vessel and the background compared to the Barker code. The optimized code exhibits a clear advantage over the Barker code for a high noise level (-30 dB). The numerical results show that the optimized code has consistent and higher SNR and CNR across different noise levels. For the noise levels 0, -15, and -30 dB, the optimized code has SNR gains of 2.33, 4.3, and 7.78 dB compared to the Barker code. The optimized code is more robust for high-level noise. The blood flow simulation result demonstrates the ability of the proposed optimized code to improve the SNR of the Doppler images in deep areas. The resolution problems exhibited by the optimized code in the previous sections are not very severe in the Doppler flow simulation.

V. Discussions and Future Work

A. Discussions

In this work, a model-based approach is embraced as it allows for more flexibility in handling the diverse coded excitation scheme used in our method. For a fair comparison between different coding schemes, we applied model-based beamforming to all coded excitations in order to ensure that any differences in performance are not due to the choice of beamforming. This approach allowed for the design of the coded excitation scheme with CRB minimization (Eig-Opt, Det-Opt, Trace-Opt) or FIM maximization (FIM-Opt). Note that the matched filter method prioritizes SNR, which is maximized by the matched filter, over spatial resolution. Therefore, all methods can suffer from slight resolution loss.

Theoretically, we can obtain the optimal solution with an exhaustive search for CRB minimization, resulting in a single transmission that captures the entire region of interest but has a high computational cost. Since the optimization problem is non-convex, convex relaxation and subsampling are used, leading to suboptimal solutions and performance degradation. A more feasible FIM-Opt approach is proposed to reduce the complexity further, providing practical solutions that approximate the ideal case, with multiple randomizations to compensate. Diverse codes ensure that different parts of the region of interest are emphasized with each transmission, producing a more comprehensive and meaningful image. This diversity benefits scenarios with multiple transmissions.

Simulations in Sections IV-A1 and IV-A2 concluded that FIM-Opt is a cost-efficient solution that performs slightly better than the Eig-Opt and Trace-Opt for the same optimization area. Besides, FIM-Opt with an enlarged optimization area outperforms the Trace-Opt and Eig-Opt optimized for a small area in terms of resolution, although FIM-Opt is still computationally more efficient.

In Section IV-A3 FIM-optimized code achieves the highest SNR and robustness to the noise and lowest CRB. However, its lower main lobe-to-side lobe ratio introduces a trade-off between SNR and resolution. For example, Barker codes are specifically designed to have good autocorrelation properties, allowing for axial resolution retrieval comparable to a single short pulse. The findings in Section IV-B1 also support these arguments. Moreover, increasing bit lengths results in higher SNR but in lower resolution and hence suffers from this trade-off. To establish a balance between SNR and resolution, LSQR is employed in Section IV-B2, and an improvement is observed until the 10th iteration for the optimized code. However, there is still a need for optimized codes that maximize the main lobe-to-side lobe ratio while minimizing CRB without using any advanced beamforming methods.

The simulation results in Section IV-C demonstrate that the optimized code offers improved SNR and CNR compared to the Barker code, again with a trade-off for the resolution. This is common in clinical imaging and often depends on the diagnostic context. For example, in scenarios where noise dominates, stronger vessel contrast can improve overall visibility, even if boundaries appear smoother. Our results indicate that small vessel visibility is not significantly compromised, as shown by the improved CNR metrics.

B. Limitations and Future Work

Our work can be considered as an initial attempt for the usage of optimized coded-excitation and it has a lot of potential for future research direction.

- As highlighted before, future work needs to achieve balanced enhancement of SNR and resolution. For example,

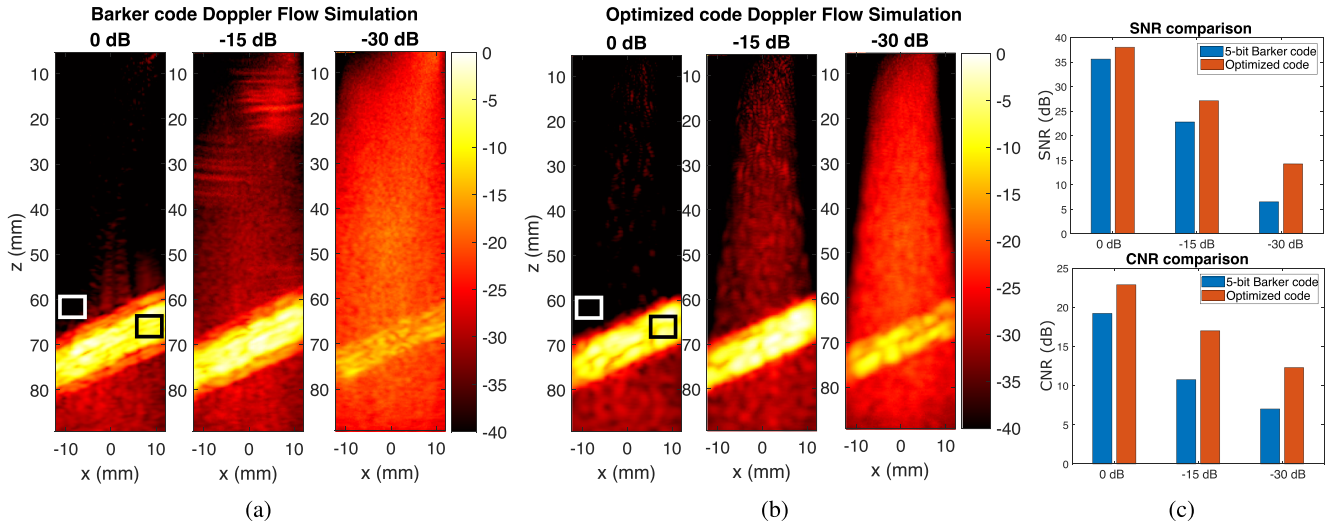

Fig. 14. (a) Power Doppler images from 5-bit Barker code with noise-to-blood levels at 0, -15, and -30 dB. (b) Power Doppler images from the optimized code. All the images are shown with the same colormap spectrum from 0 to -40 dB. (c) SNR and CNR of the Barker code and optimized code. They are calculated using the ROI shown in (a) and (b), where the black and white rectangular shows the blood vessel and the background region, respectively.

adding a resolution-related constraint (e.g., related to the autocorrelation property) to the problems in (15), (25), (22) or (29) can improve the resolution.

- This work considered amplitude encoding. However, biphase encoding can be easier to implement for more practical purposes with the Verasonics system. In the optimization function, we then need a binary constraint where $\mathbf{c} \in \{-1, 1\}^{NK}$.
- The optimization problem poses a computational complexity challenge. Future research on developing efficient algorithms rather than subsampling can be more useful.
- Another computational problem is due to the model-based approach. Although a direct application of DAS beamforming is not possible as each transmitter sends a different coded pulse, a decoding matrix for the optimized encoding matrix can be developed. Then, an initial implementation of the decoding matrix makes applying the DAS beamforming possible. Still, the design of the decoding matrix poses a computational challenge. For a similar discussion, [50] can be considered.
- Conducting *Phantom* and in Vivo experiments with the Verasonics can validate the applicability of the proposed method and are needed as future work.
- The proposed model-based framework for coded excitation can be useful for systems with compressive sensing or more advanced image reconstruction techniques with fewer sensors [51].

VI. Conclusion

In this work, we have proposed optimizing a coded excitation scheme. For this, we designed an optimized code represented by a generalized encoding matrix in a linear signal model. Then, we employed the minimization of the CRB for the unknown coding matrix. The minimization of the maximum eigenvalue, determinant, and trace of the CRB matrix has been proposed, but its computational complexity makes the optimization infeasible for a large area of interest. Therefore, instead of minimizing the trace of the CRB, maximizing the trace of the FIM has been proposed. It results in a computationally less complex problem that can be solved by finding the eigenvector of a small-sized matrix corresponding to the largest eigenvalue. We used a densely sampled high-frequency array to compare the performance of the CRB's minimization and the FIM's maximization for point scatterer data. Then, the suboptimal FIM-based method is chosen to compare its performance with the state-of-the-art. It is observed that while the SNR increases, the resolution decreases as the autocorrelation property is not considered. We also tested the suboptimal FIM-based method with a numerical model of the clinical transducer on the point scatterer data. Again, we obtained a tradeoff between SNR and resolution. We also observed that LSQR can drastically improve the resolution of the optimized code with a slight decrease in SNR. Finally, blood flow simulations are done using a clinical transducer, and the optimized code exhibits consistent and higher SNR and CNR at different noise levels. Future work highlights the need to balance SNR and resolution and computationally more efficient optimization schemes.

References

[1] R. Aaslid, T.-M. Markwalder, and H. Nornes, "Noninvasive transcranial doppler ultrasound recording of flow velocity in basal cerebral arteries," *J. Neurosurgery*, vol. 57, no. 6, pp. 769–774, 1982.

[2] S. Golemati, A. Gastounioti, and K. S. Nikita, "Toward novel noninvasive and low-cost markers for predicting strokes in asymptomatic carotid atherosclerosis: The role of ultrasound image analysis," *IEEE Trans. Biomed. Eng.*, vol. 60, no. 3, pp. 652–658, Mar. 2013.

[3] J. Bercoff et al., "Ultrafast compound doppler imaging: Providing full blood flow characterization," *IEEE Trans. Ultrason., Ferroelectr., Freq. Control*, vol. 58, no. 1, pp. 134–147, Jan. 2011.

[4] E. Mace, G. Montaldo, B.- F. Osmanski, I. Cohen, M. Fink, and M. Tanter, "Functional ultrasound imaging of the brain: Theory and basic principles," *IEEE Trans. Ultrason., Ferroelectr., Freq. Control*, vol. 60, no. 3, pp. 492–506, Mar. 2013.

[5] G. Matrone, A. Ramalli, A. S. Savoia, P. Tortoli, and G. Magenes, "High frame-rate, high resolution ultrasound imaging with multi-line transmission and filtered-delay multiply and sum beamforming," *IEEE Trans. Med. Imag.*, vol. 36, no. 2, pp. 478–486, Feb. 2017.

[6] J. Luo, R. X. Li, and E. E. Konofagou, "Pulse wave imaging of the human carotid artery: An in vivo feasibility study," *IEEE Trans. Ultrason., Ferroelectr., Freq. Control*, vol. 59, no. 1, pp. 174–181, Jan. 2012.

[7] E. Sassaroli, C. Crake, A. Scorza, D.-S. Kim, and M.-A. Park, "Image quality evaluation of ultrasound imaging systems: Advanced B-modes," *J. Appl. Clin. Med. Phys.*, vol. 20, no. 3, pp. 115–124, 2019.

[8] J. U. Kidav, N. Sivamangai, M. Pillai, and S. Sreejeesh, "A broadband MVDR beamforming core for ultrasound imaging," *Integration*, vol. 81, pp. 221–233, 2021.

[9] M. A. S. Christopher and C. Paige, "LSQR: An algorithm for sparse linear equations and sparse least squares," *ACM Trans. Math. Softw.*, vol. 8, no. 1, pp. 43–71, 1982.

[10] D. Dogan, P. Kruizinga, J. G. Bosch, and G. Leus, "Multiple measurement vector model for sparsity-based vascular ultrasound imaging," in *Proc. 2021 IEEE Stat. Signal Process. Workshop (SSP)*, 2021, pp. 501–505.

[11] B. Luijten et al., "Adaptive ultrasound beamforming using deep learning," *IEEE Trans. Med. Imag.*, vol. 39, no. 12, pp. 3967–3978, Dec. 2020.

[12] C. Demené et al., "Spatiotemporal clutter filtering of ultrafast ultrasound data highly increases doppler and fUltrasound sensitivity," *IEEE Trans. Med. Imag.*, vol. 34, no. 11, pp. 2271–2285, Nov. 2015.

[13] Y. Liu, Y. Yang, Y. Shu, T. Zhou, J. Luo, and X. Liu, "Super-resolution ultrasound imaging by sparse Bayesian learning method," *IEEE Access*, vol. 7, pp. 47197–47205, 2019.

[14] A. Bar-Zion, O. Solomon, C. Tremblay-Darveau, D. Adam, and Y. C. Eldar, "SUSHI: Sparsity-based ultrasound super-resolution hemodynamic imaging," *IEEE Trans. Ultrason., Ferroelectr., Freq. Control*, vol. 65, no. 12, pp. 2365–2380, Dec. 2018.

[15] T. Misaridis and J. A. Jensen, "Use of modulated excitation signals in medical ultrasound. Part I: Basic concepts and expected benefits," *IEEE Trans. Ultrason., Ferroelectr., Freq. Control*, vol. 52, no. 2, pp. 177–191, Feb. 2005.

[16] T. Misaridis and J. A. Jensen, "Use of modulated excitation signals in medical ultrasound. Part II: Design and performance for medical imaging applications," *IEEE Trans. Ultrason., Ferroelectr., Freq. Control*, vol. 52, no. 2, pp. 192–207, Feb. 2005.

[17] T. Misaridis and J. A. Jensen, "Use of modulated excitation signals in medical ultrasound. Part III: High frame rate imaging," *IEEE Trans. Ultrason., Ferroelectr., Freq. Control*, vol. 52, no. 2, pp. 208–219, Feb. 2005.

[18] E. P. Vienneau and B. C. Byram, "A coded excitation framework for high SNR transcranial ultrasound imaging," *IEEE Trans. Med. Imag.*, vol. 42, no. 10, pp. 2886–2898, Oct. 2023.

[19] A. Nowicki, J. Tasinkiewicz, and I. Trots, "Flow imaging using differential golay encoded ultrasound," *Ultrasonics*, vol. 126, 2022, Art. no. 106825.

[20] C. Yoon, W. Lee, J. H. Chang, T.-K. Song, and Y. Yoo, "An efficient pulse compression method of chirp-coded excitation in medical ultrasound imaging," *IEEE Trans. Ultrason., Ferroelectr., Freq. Control*, vol. 60, no. 10, pp. 2225–2229, Oct. 2013.

[21] V. Behar and D. Adam, "Parameter optimization of pulse compression in ultrasound imaging systems with coded excitation," *Ultrasonics*, vol. 42, no. 10, pp. 1101–1109, 2004.

[22] R. Y. Chiao and X. Hao, "Coded excitation for diagnostic ultrasound: A system developer's perspective," *IEEE Trans. Ultrason., Ferroelectr., Freq. Control*, vol. 52, no. 2, pp. 160–170, Feb. 2005.

[23] H. Zhao, L. Y. L. Mo, and S. Gao, "Barker-coded ultrasound color flow imaging: Theoretical and practical design considerations," *IEEE Trans. Ultrason., Ferroelectr., Freq. Control*, vol. 54, no. 2, pp. 319–331, Feb. 2007.

[24] I. A. Veres et al., "Golay code modulation in low-power laser-ultrasound," *Ultrasonics*, vol. 53, no. 1, pp. 122–129, 2013.

[25] I. Trots, "Mutually orthogonal Golay complementary sequences in synthetic aperture imaging systems," *Arch. Acoust.*, vol. 40, no. 2, pp. 283–289, 2015.

[26] P. Ni and H.-N. Lee, "High-resolution ultrasound imaging using random interference," *IEEE Trans. Ultrason., Ferroelectr., Freq. Control*, vol. 67, no. 9, pp. 1785–1799, Sep. 2020.

[27] M. Tamraoui, H. Liebgott, and E. Roux, "Complete complementary coded excitation scheme for SNR improvement of 2D sparse array ultrasound imaging," *IEEE Trans. Biomed. Eng.*, vol. 71, no. 3, pp. 1043–1055, Mar. 2024.

[28] Z. Fan, J. Rudlin, G. Asfis, and H. Meng, "Convolution of barker and golay codes for low voltage ultrasonic testing," *Technologies*, vol. 7, no. 4, 2019, Art. no. 72.

[29] Y. M. Benane, D. Bujoreanu, C. Cachard, B. Nicolas, and O. Basset, "An enhanced chirp modulated golay code for ultrasound diverging wave compounding," in *Proc. 26th Eur. Signal Process. Conf. (EUSIPCO)*, IEEE, 2018, pp. 81–85.

[30] C.-H. Hu, R. Liu, Q. Zhou, J. Yen, and K. Kirk Shung, "Coded excitation using biphase-coded pulse with mismatched filters for high-frequency ultrasound imaging," *Ultrasonics*, vol. 44, no. 3, pp. 330–336, 2006.

[31] K. B. Eom, "Speckle reduction in ultrasound images using non-isotropic adaptive filtering," *Ultrasound in Med. Biol.*, vol. 37, no. 10, pp. 1677–1688, 2011.

[32] E. P. Vienneau and B. C. Byram, "A coded excitation framework for increased signal-to-noise ratio of in vivo ultrasound power doppler imaging," in *Medical Imaging 2021: Ultrasonic Imaging and Tomography*, Bellingham, WA, USA: SPIE, 2021, pp. 146–152.

[33] E. Grossi, M. Lops, L. Venturino, and A. M. Tulino, "Robust waveform design for MIMO radars," in *Proc. 2010 IEEE Int. Symp. Inf. Theory*, 2010, pp. 1633–1637.

[34] H. Xu, J. Zhang, W. Liu, S. Wang, and C. Li, "High-resolution radar waveform design based on target information maximization," *IEEE Trans. Aerosp. Electron. Syst.*, vol. 56, no. 5, pp. 3577–3587, Oct. 2020.

[35] T. Schonhoff and A. Giordano, *Detection and Estimation Theory and its Applications*. Upper Saddle River, NJ, USA: Pearson Prentice Hall, 2006.

[36] P. van der Meulen, P. Kruizinga, J. G. Bosch, and G. Leus, "Coding mask design for single sensor ultrasound imaging," *IEEE Trans. Comput. Imag.*, vol. 6, pp. 358–373, 2019.

[37] J. Li, L. Xu, P. Stoica, K. W. Forsythe, and D. W. Bliss, "Range compression and waveform optimization for MIMO radar: A Cramér–Rao bound based study," *IEEE Trans. Signal Process.*, vol. 56, no. 1, pp. 218–232, Jan. 2008.

[38] S. Boyd and L. Vandenberghe, "Semidefinite programming relaxations of non-convex problems in control and combinatorial optimization," in *Communications, Computation, Control, and Signal Processing: A Tribute to Thomas Kailath*, Berlin, Germany: Springer, 1997, pp. 279–287.

[39] J. T. Fokkema and P. M. van den Berg, *Seismic Applications of Acoustic Reciprocity*. Amsterdam, The Netherlands: Elsevier, 1993.

[40] R. Lavarello, F. Kamalabadi, and W. O'Brien, "A regularized inverse approach to ultrasonic pulse-echo imaging," *IEEE Trans. Med. Imag.*, vol. 25, no. 6, pp. 712–722, Jun. 2006.

[41] M. A. Richards, J. A. Scheer, W. A. Holm, and W. L. Melvin, *Principles of Modern Radar: Basic Principles*. Raleigh, NC, USA: SciTech, 2010.

[42] A. Saumard and J. A. Wellner, "Log-concavity and strong log-concavity: A review," *Statist. Surv.*, vol. 8, pp. 45–114, 2014.

[43] J. Gallier et al., "The Schur complement and symmetric positive semidefinite (and definite) matrices," Dept. Comput., Tech. Rep. MS-CIS-10-19, 2010.

[44] Z.-Q. Luo, W.-K. Ma, A. M.-C. So, Y. Ye, and S. Zhang, "Semidefinite relaxation of quadratic optimization problems," *IEEE Signal Process. Mag.*, vol. 27, no. 3, pp. 20–34, May 2010.

[45] E. Feron, "Nonconvex quadratic programming, semidefinite relaxations and randomization algorithms in information and decision systems," in *System Theory: Modeling, Analysis and Control*, Berlin, Germany: Springer, 2000, pp. 255–274.

[46] M. Grant, S. Boyd, and Y. Ye, "CVX: Matlab software for disciplined convex programming," CVX Res., Inc., 2009. [Online]. Available: http://cvxr.com/cvx

[47] D. P. Bertsekas, *Constrained Optimization and Lagrange Multiplier Methods*. Cambridge, MA, USA: Academic Press, 2014.

[48] B. E. Treeby and B. T. Cox, "k-wave: MATLAB toolbox for the simulation and reconstruction of photoacoustic wave fields," *J. Biomed. Opt.*, vol. 15, no. 2, pp. 021314–021314, 2010.

[49] J. Levy, D. L. Barrett, N. Harris, J. J. Jeong, X. Yang, and S. C. Chen, "High-frequency ultrasound in clinical dermatology: A review," *Ultrasound J.*, vol. 13, pp. 1–12, 2021.

[50] N. Bottenus, J. Spainhour, and S. Becker, "Comparison of spatial encodings for ultrasound imaging," *IEEE Trans. Ultrason., Ferroelectr., Freq. Control*, vol. 70, no. 1, pp. 52–63, Jan. 2023.

[51] Y. Hu et al., "Compressive imaging with spatial coding masks on low number of elements: An emulation study," in *Proc. 2022 IEEE Int. Ultrasonics Symp. (IUS)*, 2022, pp. 1–4.